Exploring Seebeck-coefficient fluctuations in endohedral-fullerene, single-molecule junctions.

Supporting Information

Ali K. Ismael[1,2, ∃,*], Laura Rincón-García[3, ∃], Charalambos Evangeli[4, ∃], Panagiotis Dallas[5,6, ∃], Turki Alotaibi[1,7, ∃], Alaa A. Al-Jobory[1,8, ∃], Gabino Rubio-Bollinger[3,9], Kyriakos Porfyrakis[6], Nicolás Agraït[3,9, 10,*] and Colin J. Lambert[1,*]

[1] Department of Physics, Lancaster University, Lancaster, United Kingdom.

[2] Department of Physics, College of Education for Pure Science, Tikrit University, Tikrit, Iraq.

[3] Departamento de Física de la Materia Condensada, Universidad Autónoma de Madrid, E-28049 Madrid, Spain.

[4] Department of Materials, University of Oxford, Parks Road, OX1 3PH, Oxford, United Kingdom.

[5] Institute of Nanoscience and Nanotechnology, NCSR Demokritos, 15310 Athens, Greece.

[6] Department of Materials, University of Oxford, OX1 3PH, United Kingdom.

[7] Department of Physics, College of Science, Jouf University, Sakaka, Saudi Arabia.

[8] Department of Physics, College of Science, University of Anbar, Anbar, Iraq.

[9] Condensed Matter Physics Center (IFIMAC) and Instituto Universitario de Ciencia de Materiales "Nicolás Cabrera" (INC), Universidad Autónoma de Madrid, E-28049 Madrid, Spain.
[10] Fundación IMDEA Nanociencia, Calle Faraday 9, Campus Universitario de Cantoblanco, E-28049 Madrid, Spain.

Contents

Section 1: Purification of the fullerene samples.

Synthesis and purification of the EMFs: For the synthesis of $Sc_3C_2@C_{80}$, the arc discharge vaporization of composite graphite method was employed. In a typical experiment, graphite rods doped with Sc_2O_3 (0.8 % wt, Toyo Tanso, Japan) were vaporized under 80 mbar of constant helium flow and a dc current of 500 amps. The polarity of the dc current was changing after each arc. The carbon soot was collected and Soxhlet extracted with toluene for 48 hours. The different fullerenes were separated through HPLC. The trimetallic nitride endohedral metallofullerenes (TNT EMFs), $Er_3N@C_{80}$ and $Sc_3N@C_{80}$, were purchased from SES Research Inc. and were purified with HPLC and tested with mass spectroscopy prior to further use.

Characterization techniques: The purification of the crude extract and the TNT EMFs was performed with HPLC chromatography using a Cosmosil Buckyprep M column, 20 × 250 mm (Nacalai Tesque). Toluene was used as the eluent phase and the flow rate was 14 ml/min for all experiments. Calibration curves based on $Y@C_{82}$ were used to estimate the yield of the reaction procedure. The purity of the samples was tested through matrix-assisted laser-desorption ionization time-of-flight mass spectra (MALDI-TOF MS-negative ionization) that were recorded on a Bruker MALDI-TOF spectrometer using dithranol in either positive or negative ionization mode. UV-Visible spectra were recorded on a Jasco spectrometer in o-dichlorobenzene solutions.

Section 2: Mass spectrometry.

High performance liquid chromatography was employed for the purification of all endohedral fullerenes. We present a typical HPLC graph for the isolation of $Sc_3C2@C_{80}$ in Figure S1. The $Sc_3C_2@C_{80}$, appears at a high retention time of more than 24 minutes, clearly distinguishing itself for the dimetallic counterpart $Sc_2C_2@C_{80}$. The empty cage fullerenes appear in significantly shorter retention times.
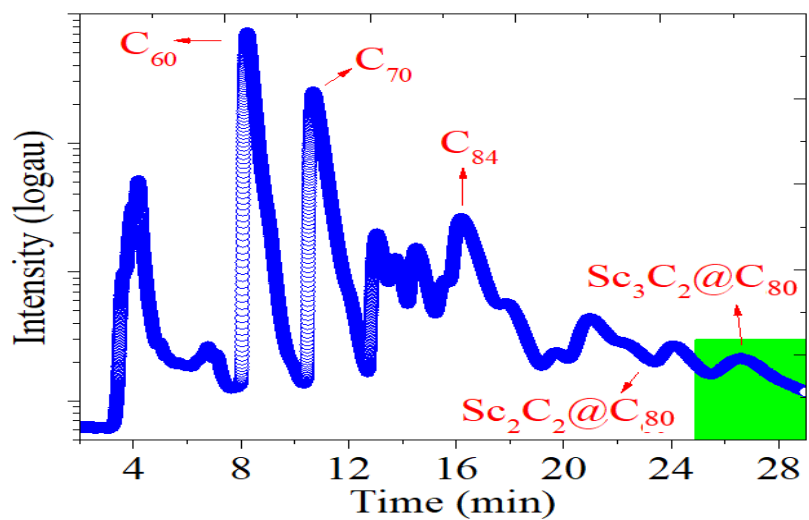
Figure S1. HPLC graph of the crude extract, derived from the vaporization of scandium containing graphite rods. The peak at retention time 25-28 minutes corresponding to the $Sc_3C_2@C_{80}$ is indicated, as also the peaks corresponding to other empty cage and endohedral fullerenes.
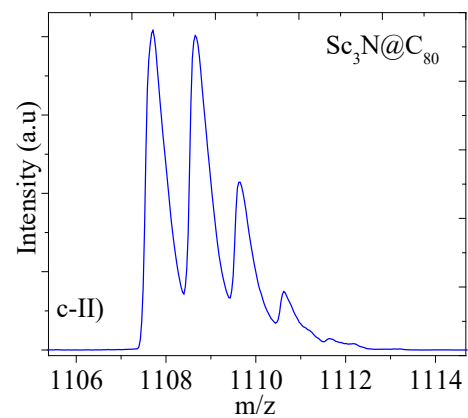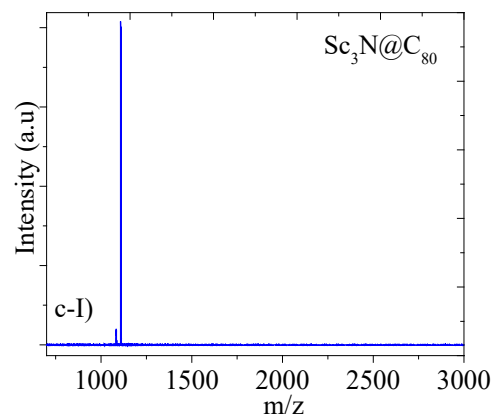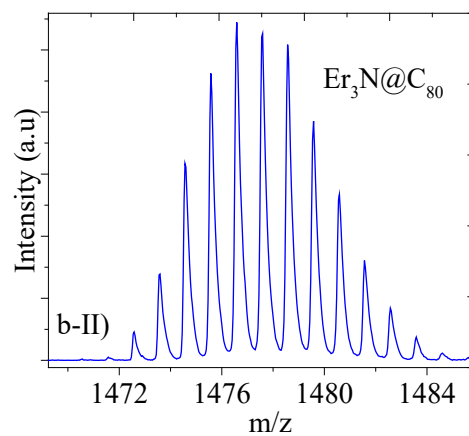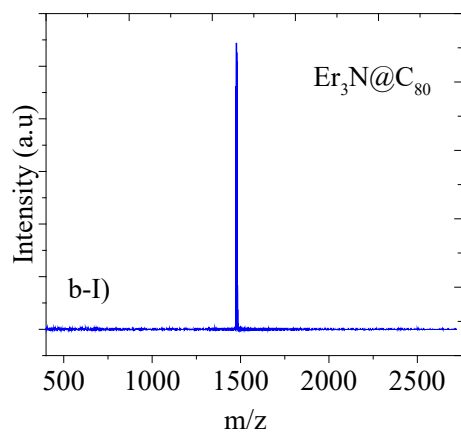
750   1500   2250   3000

Negative

Sc₃C₂@C₈₀

Positive

a-I)

750   1500   2250   3000

m/z

a-II)

1119 1120 1121 1122 1123 1124

m/z

Er₃N@C₈₀

b-I)

500   1000   1500   2000   2500

m/z

Er₃N@C₈₀

b-II)

1472   1476   1480   1484

m/z

Sc₃N@C₈₀

c-I)

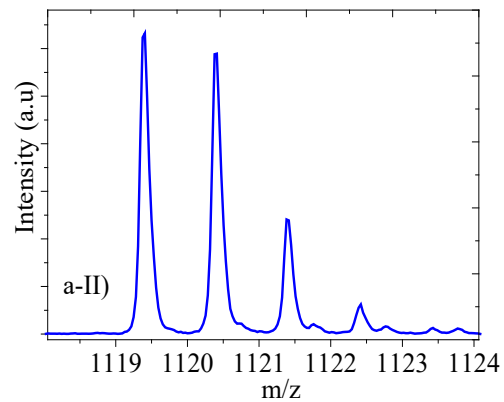1000 1500 2000 2500 3000

m/z

Sc₃N@C₈₀

c-II)

1106 1108 1110 1112 1114

m/z

4

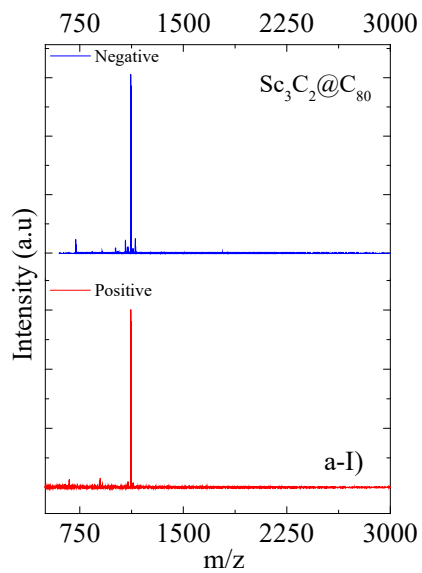**Figure S2.** MALDI-TOF spectra of the a) $Sc_3C_2@C_{80}$ in either positive (red) or negative (blue) ionization mode b) $Er_3N@C_{80}$ c) $Sc_3N@C_{80}$.

Section 3: Spectroscopic characterization and band gap calculation.

In Figure S3 we present the UV-Visible spectra (Figure S3a) for the two TNTs that were recorded in o-dichlorobenzene solutions. The direct optical band gaps of the two trimetallic nitride endohedral metallofullerenes were calculated from the Tauc plots that can be seen in Figure S3b. The energy of the transition, in eV, is plotted against $(\alpha h\nu)^{1/r}$. For a direct allowed transition, we consider a value of r=1/2. Consequently, the band gaps are calculated to be 2.466 eV for $Sc_3N@C_{80}$ and 2.54 eV for $Er_3N@C_{80}$ from the fitting of the Tauc plot.

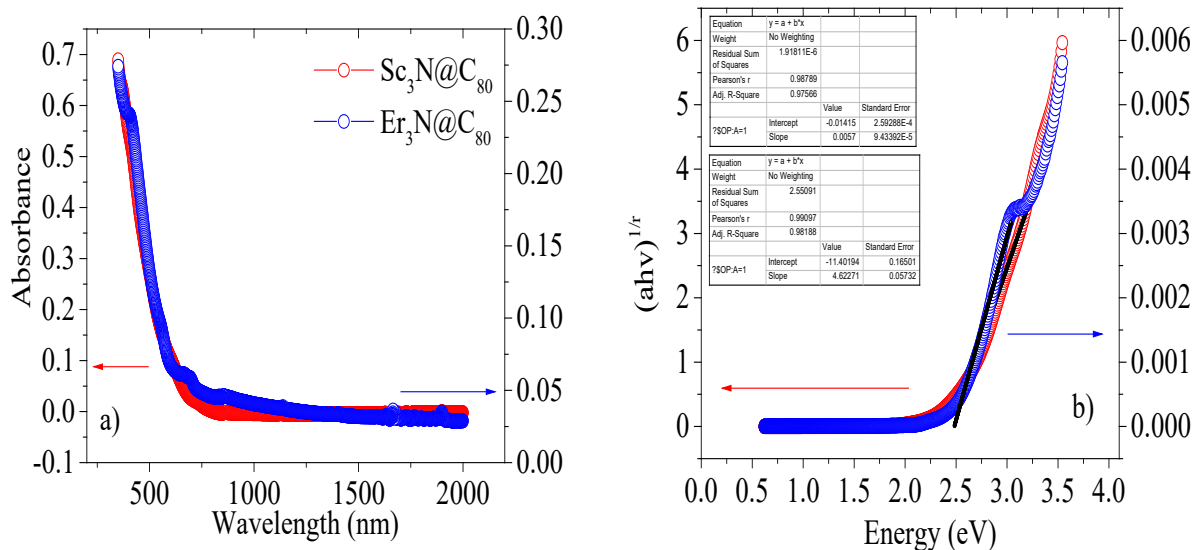**Figure S3.** UV-Visible absorbance spectra (a) and Tauc plots (b) recorded in o-dichlorobenzene solutions for $Er_3N@C_{80}$ (blue) and $Sc_3N@C_{80}$ (red). The direct, optical band gaps, taking into consideration a value for r=1/2 are: 2.54 eV for $Er_3N@C_{80}$ and 2.46 eV for $Sc_3N@C_{80}$. The values are calculated from a fitting on the linear regime of the Tauc plot.

MALDI-TOF data are providing invaluable information for the formation of endohedral metallofullerenes species, however, they do not provide with a definite proof on the structure of the buckyball and the species incarcerated within. To that end, we recorded the EPR spectra and they demonstrated the unique diamond

shape with 22 lines that arises from three equivalent scandium nuclei. The spectra for the temperature range 170—290 K can be seen in Figure S4.
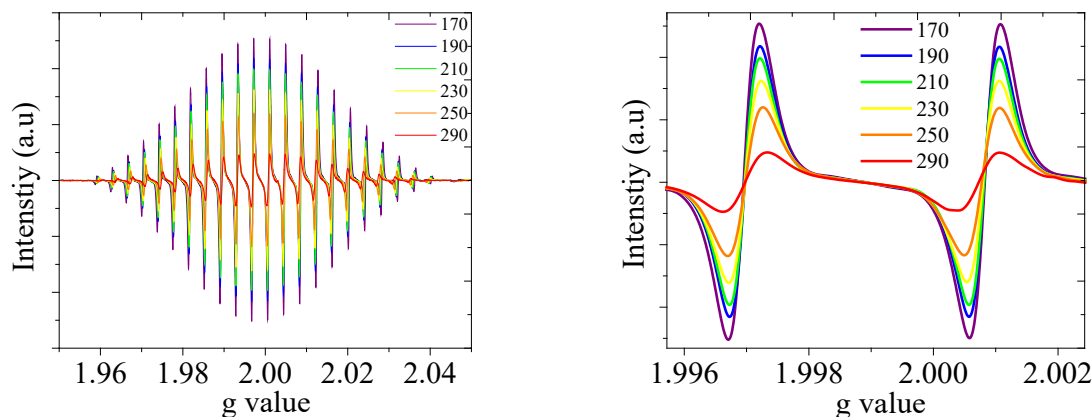

Figure S4. EPR spectra of the paramagnetic $Sc_3C_2@C_{80}$ recorded at various temperatures (170-290 K). The 22 lines stemming from three equivalent scandium (I=7/2) nuclei demonstrate the unambiguous synthesis of the trimetallic carbide.

Section 4: Experimental details.

4.1. Sample preparation and experimental technique

Samples are prepared by depositing the endohedral metallofullerene of interest on a 250-nm-thick Au film on a glass substrate (11×11 mm^2, Arrandee, Germany). The gold surface is flame annealed prior to the molecule deposition to have clean gold reorganized in a polycrystalline (111) surface. The sample is afterwards allowed to cool down to room temperature and the molecules are then deposited using the drop-casting technique. EMFs are initially in solid state (powder) and need to be diluted to get low coverages of the Au surface. Proceeding in several steps, we prepare a very dilute EMF solution in 1,2,4-trichlorobenzene (TCB) (>99%, Sigma-Aldrich) of around $10^{-7} - 10^{-8}$ M and place a drop on the pre-annealed Au surface for about three minutes. We finally blow it off with streaming nitrogen and allow the sample to dry overnight in ambient conditions.

The experimental setup employed in our experiments is a scanning tunnelling microscope (STM) operated in ambient conditions and at room temperature. Once the sample is mounted on the STM, it is also let to stabilize for around an hour to reach thermal equilibrium with the setup and minimize the thermal drift. Complementary, we use mechanically cut Au tips as STM probes (Goodfellow, 0.25-nm-diameter, 99.99% purity). The STM is a home-built setup that has been adapted to measure simultaneously the conductance and thermopower of nanoscale junctions.[1] The major modification introduced in the standard STM setup is the addition of a surface mount 1 kΩ resistor on the tip support which acts as a heater for the tip, which is in good thermal contact with the back of the resistor. On the other, the substrate is maintained at room temperature T_c and hence a temperature difference $\Delta T = T_h - T_c$ between the tip and the sample is established, where T_h is the temperature of the tip, and $T_h > T_c$. Two thermocouples (placed on the heating resistor and on the sample) allow us to monitor the resulting ΔT, which ranges from around 30 K to 40 K for the experiments reported here. When applying a temperature difference, we found that the temperature stabilizes in about 15-30 minutes and that the thermal drift increases, making it necessary to use fast imaging to locate the isolated molecules as an essential part of the experimental technique, as it is introduced next.

The experimental technique employed consists mainly of three steps: scanning of the sample surface to localize individual molecules, by means of STM-images; connection of the molecule forming a molecular junction and simultaneous measurement of G and S, and second acquisition of STM-images to monitor possible modifications of the molecule position.

First, the use of STM images prior to junction formation is one of the major requirements of the experiments performed since it is essential to precisely know the number of molecules involved in the junction. Examples of these images, which also confirm the correct deposition of the EMFs on the Au surface, can be found in the main paper and in the next section.

Secondly, once a single molecule is targeted, both conductance G and thermopower S can be simultaneously measured doing small voltage ramps during the approach and retraction of the STM tip with respect to the molecule, as described in Figure S5. During the tip motion, the bias voltage V_{bias} applied to the sample is kept constant at a given value $V_0 = 10$ mV, (plotted in blue in Figure S5a,b). Every few picometers $(15 - 25$ pm) the tip motion is stopped and the bias voltage is ramped between $\pm V_0$ while the tip is stationary (in red in Figure S5a,b). These low-voltage I-V traces show linear ohmic behaviour, proving good coupling of the molecule to the electrodes, and when no temperature difference is applied between both STM electrodes, i.e. $\Delta T = 0$ K, $I = 0$ takes place at zero bias voltage (see Figure S5c). On the contrary, when a non-zero temperature difference is established between tip and sample, the I-V curves show a ΔT-dependent voltage offset at zero current (see Figure S5c), which correspond to the thermovoltage of the system.
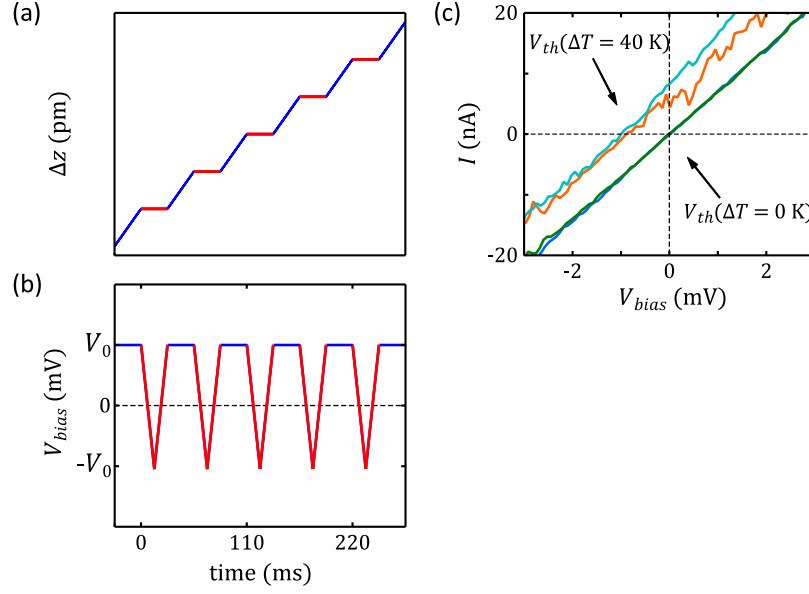
Figure S5. Technique for the simultaneous measurement of conductance G and thermopower S. a,b) Tip displacement Δz and applied bias voltage V_{bias}, respectively, as a function of time. The bias voltage is maintained at a fixed value V_0 during the tip motion (in blue) and every few picometers it is swept between $\pm V_0$ while the tip is stationary (in red). c) Examples of experimental I-V traces, zooming for voltage values close to zero. In the presence of a temperature difference $\Delta T \neq 0$ K, a voltage offset V_{th} appears at zero current.

It is important to have in mind that heating the tip translates into a temperature difference established not only between tip and sample but also across the tip-connecting lead, which gives rise to an additional thermoelectric signal that needs to be considered (see Figure S6). The total thermovoltage V_{th} measured in the I-V traces contains then both contributions, from the junction and from the lead. Considering the equivalent thermal-electric circuit of the system depicted in Figure S6, the current through the STM junction can be written as:

$$I = G[V_{bias} + S\Delta T - S_{lead}\Delta T] = G[V_{bias} + V_{th}]$$

where I is the electrical current through the junction; V_{bias} and ΔT are the applied bias voltage and temperature difference, respectively; G and S are the conductance and thermopower of the junction, respectively; S_{lead} is the thermopower of the tip-connecting lead, which in our system is a copper wire (thus, $S_{lead} = 1.83\ \mu V/K$),[2] and V_{th} is the total thermovoltage, which can be written as $V_{th} = (S - S_{lead})\Delta T$. This is directly the ΔT-dependent voltage offset measured at zero current with the I-V traces. In practice, the application of this expression allows us to measure simultaneously both the conductance and the thermopower: measuring V_{th} and ΔT the thermopower of the junction S is straightforwardly calculated and, in addition and simultaneously, the slope of the I-V curve corresponds to the conductance G of the junction. In each approach-retraction cycle, approximately 50-100 I-V curves are typically acquired, giving as many values of the conductance and the Seebeck coefficient.
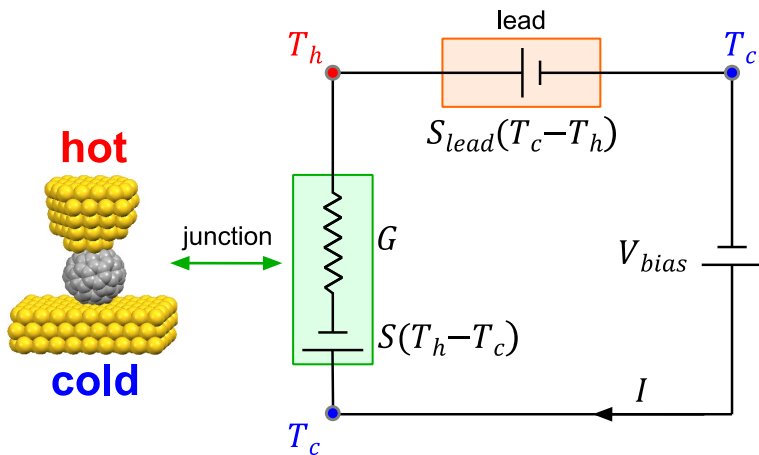

Figure S6. Equivalent thermal-electric circuit. The STM tip is heated to a temperature T_h above ambient temperature (in red), while the substrate is maintained at ambient temperature T_c (in blue), establishing a temperature difference $\Delta T = T_h - T_c$ that generates a thermoelectric response both in the STM junction (in green) and in the tip-connecting lead (in orange). S and S_{lead} are their corresponding Seebeck coefficients. Other elements considered in the circuit are the bias voltage applied to the substrate (V_{bias}), the current flowing through the STM junction (I) and its electrical conductance (G).

Finally, STM images of the area around the connected molecule are acquired after the junction formation to monitor possible modifications of the molecule position. If it remains stable after junction formation, the technique enables to perform further transport measurements in the very same molecule by successive approach-retraction cycles of the tip.

4.2. STM images of EMFs on Au(111)

STM images of the Au surface and the EMFs adsorbed on it are acquired at room temperature and in constant-current mode with the bias voltage V_{bias} applied to the sample (typically several hundreds of mV,

between 300 and 800 mV). A commercial current-to-voltage amplifier Keithley 428 is used, with a gain of 10^8 V/A, and a tunnelling current of $\sim$1 nA is set to control the vertical piezo position and scan the surface.

Figure 1 in the main paper and Figure S7 show representative examples of STM images of the two "new" EMFs investigated, i.e. $Sc_3C_2@C_{80}$ and $Er_3N@C_{80}$, deposited on Au(111). STM images of $Sc_3N@C_{80}$ molecules deposited on Au(111) can be found in Ref.[3] Thanks to the low molecule concentration of the solutions prepared, we can easily localize areas on the Au surface where isolated EMFs have adsorbed, preferentially at monoatomic steps but also on flat terraces (Figure S7c, for example). Preferred bonding at step edges is to be expected since they are more reactive sites and Au atoms at these positions have more dangling bonds, favouring the adsorption of the electron acceptor molecules. In fact, covalent bonding of the EMFs is taking place, with hybridization of the molecular orbitals and the extended electronic states of the metal surface and a net charge transfer from the electron-rich substrate towards the molecule. Most of the EMFs contacted in our experiments are indeed sitting at step edges.
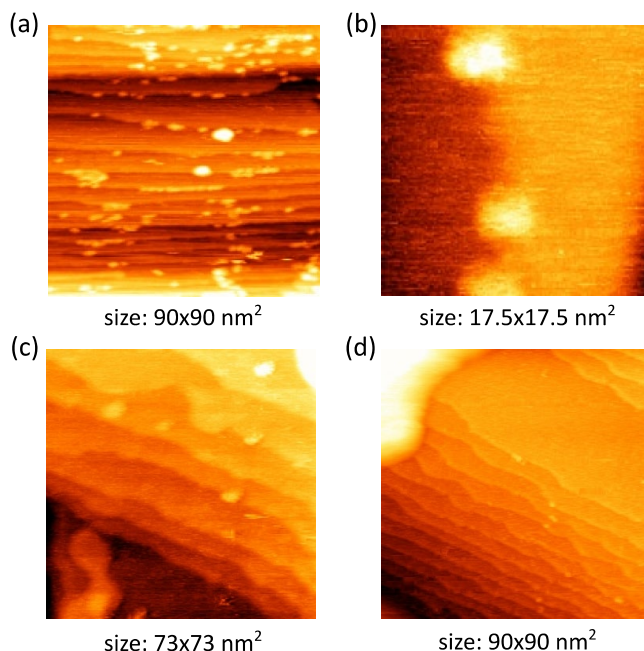
(a)

size: 90x90 nm^2

(b)

size: 17.5x17.5 nm^2

(c)

size: 73x73 nm^2

(d)

size: 90x90 nm^2

Figure S7. STM-images of $Sc_3C_2@C_{80}$ (a,b) and $Er_3N@C_{80}$ (c,d) molecules deposited on Au(111), showing adsorption of the EMFs at step edges (preferred) and flat terraces, both as isolated molecules and small islands. Images treated with the Gwyddion software.[4]

In summary, STM images of EMFs deposited on polycrystalline Au substrates show stable adsorption of the molecules with submonolayer coverages. Despite not being able to obtain intramolecular resolution, molecules seem to do not suffer any bonding-induced structural damage, they are generally well anchored

to the metallic surface although certain tip-induced mobility is sometimes observed and they show a clear preference to attach to monoatomic step edges.

4.3. Further examples of individual simultaneous measurements of conductance G and thermopower S for Sc$_3$C$_2$@C$_{80}$ and Er$_3$N@C$_{80}$ single-molecule junctions
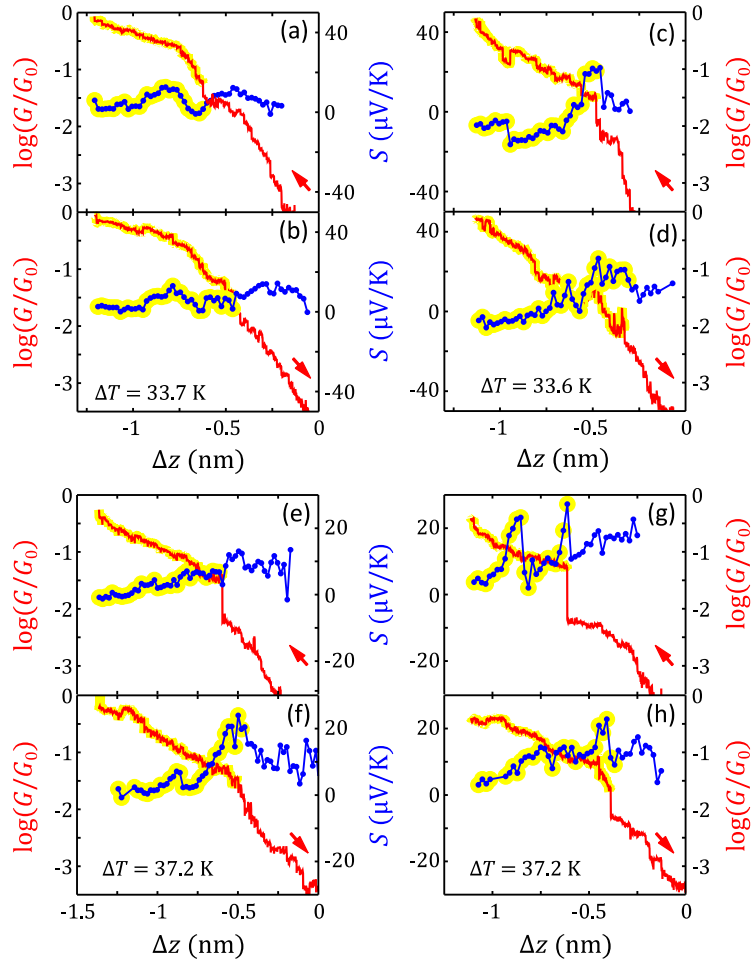

Figure S8. Examples of individual simultaneous measurements of conductance G and thermopower S of Sc$_3$C$_2$@C$_{80}$ (a-d) and Er$_3$N@C$_{80}$ (e-h) junctions. These curves correspond to four examples of approach (a,c,e,g) and retraction (b,d,f,h) cycles on single-molecule junctions where the conductance G (in red) and thermopower S (in blue) are simultaneously acquired. The first Sc$_3$C$_2$@C$_{80}$ junction in a-b presents a small positive thermopower and shows correlation between G and S changes, while the second Sc$_3$C$_2$@C$_{80}$ junction in c-d exhibits initially a positive thermopower that undergoes a change of sign as the tip keeps approaching. Finally, Er$_3$N@C$_{80}$ molecules in e-f and g-h present positive Seebeck coefficients. Two large abrupt jumps in S are observed in the approach trace of the fourth junction (g-h) correlated with changes in G: the first jump in S is correlated with the rapid increase in G signalling contact-formation and the second one is correlated with a small jump down in G and a subtle change in the slope, possibly indicating local atomic rearrangements in the tip. The temperature difference ΔT is indicated in each measurement and the portion of G and S corresponding to the contact regime is highlighted in yellow.

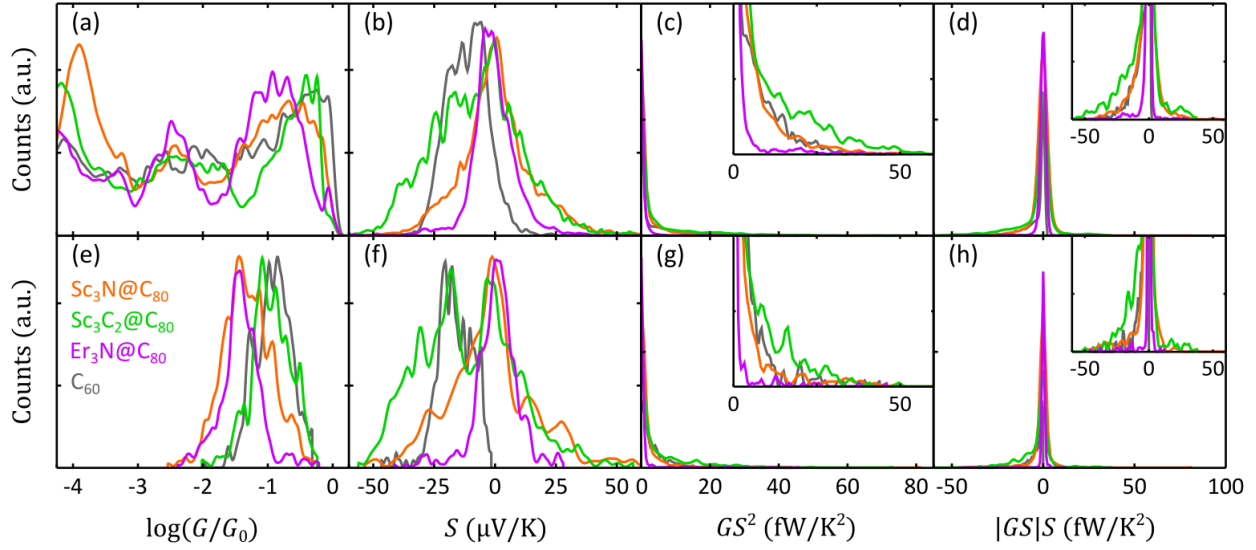## 4.4. G, S, and GS^2 1D histograms for single-molecule junctions

Figure S9. Conductance G, thermopower S and power factor GS^2 and $|GS|S$ 1D histograms of the monomers of EMFs and C_{60}. a-d) Histograms built with all the data from the I-V curves measured during the complete approach of the tip, from the noise level until close to the metallic contact. e-h) Histograms built only with first-contact values, i.e., within 0.1 nm after junction formation. Insets in c-d and g-h zoom into the details of the power factor data presented in the main panel. $|GS|S$ 1D histograms (d and h) are shown to highlight the asymmetry due to positive and negative thermopower values. Panels e), f) and g) are those shown in Figures 3 and 6a.
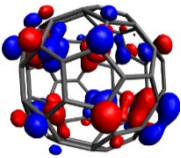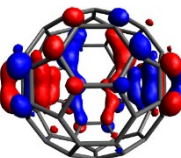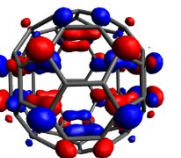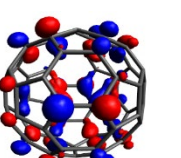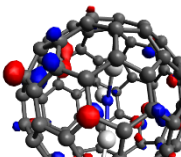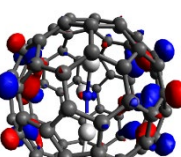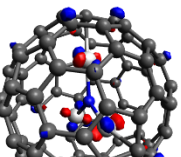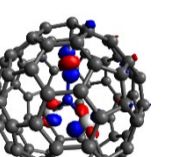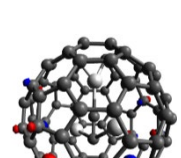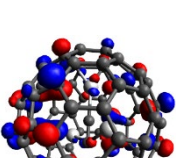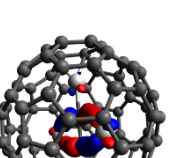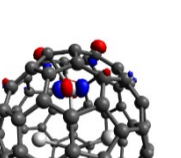
Section 5: Theoretical details.

5.1. Frontier orbitals of the EMFs molecules and the C_{60}
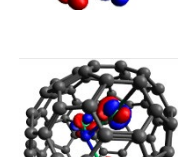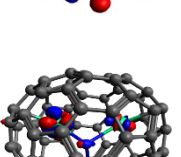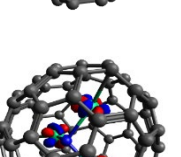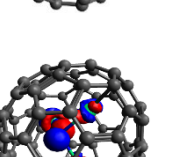
Table S1 shows the frontier orbitals of the studied molecules, obtained using the DFT code SIESTA.[5] The optimum geometries of the isolated molecules were obtained by relaxing the molecules until all forces on the atoms were less than 0.05 eV/Å. A double-zeta plus polarization orbital basis set, norm-conserving pseudopotentials were utilised, an energy cutoff of 200 Rydbergs defined the real space grid and the local density approximation (LDA) was chosen to be the exchange correlation functional. We also computed results using GGA and found that the resulting transmission functions were comparable with those obtained using LDA.[6-8]

Table S1 shows the theoretical frontier orbitals of the isolated molecules. DFT tends to underestimate the HOMO-LUMO gap,[9, 10] which is why the calculated gaps in Table S1 are smaller than the optically-measured gaps in Figure S3.

Table S1. Comparison between the frontier molecular orbitals of C_{60} and EMFs in the gas phase.

Molecule	E_F (eV)	HOMO-1	HOMO	LUMO	LUMO+1	E (eV)
C_{60}	-4.13					HOMO-1 = -4.80 HOMO = -4.80 LUMO = -3.13 LUMO+1 = -3.13
$Sc_3N@C_{80}$	-3.58					HOMO-1 = -4.45 HOMO = -4.35 LUMO = -2.83 LUMO+1 = -2.55
$Sc_3C_2@C_{80}$	-3.89					HOMO-1 = -4.39 HOMO = -4.36 LUMO = -3.89 LUMO+1 = -2.97
$Er_3N@C_{80}$	-3.91					HOMO-1 = -3.95 HOMO = -3.94 LUMO = -3.84 LUMO+1 = -3.74

5.2. Axes and rotation modes of EMFs

There are an infinite number of inequivalent orientations of the metallic moiety relative to the fullerene cage. Here we consider a selection of rotations about high-symmetry axes. Figure S10 shows four axes of rotation θ, Φ, α and β considered below. Figure S11 shows how these axes pass through the metallic moieties. For each of the four axes of rotation, we investigate how the total energy varies with angle of rotation, both in presence and absence of the gold substrate. For each of these four axes, we consider one mode of rotation in the gas phase and three modes of rotation on a substrate.

In the gas phase, we consider rotation of the metallic moiety relative to a fixed fullerene cage. For this rotational mode, rotations about the β and Φ axes are equivalent, so in total we consider 3 distinct axes of rotation. In the presence of the gold substrate, we consider three modes of rotation about each of the four axes: rotation of the bare metallic moiety (in the absence of the cage), rotation of the metallic moiety in the presence of a fixed cage and rotation of both the metallic moiety and cage, such that their relative orientation is fixed. This means that in total, on a substrate, we consider 12 distinct cases (4 axes x 3 modes of rotation).
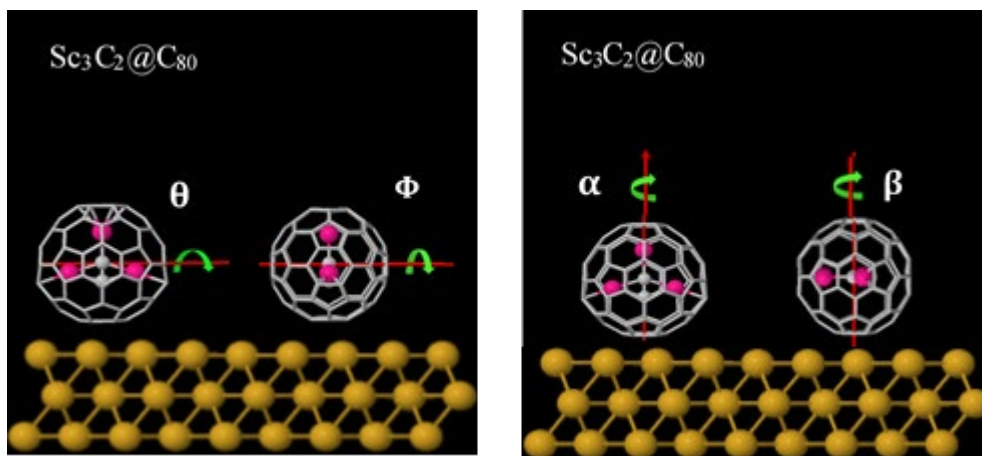

Figure S10. Illustration of the four rotation axes: θ, Φ are horizontal axes, α and β are vertical axes. This Figure shows how the axes pass through the I_h-C_{80} cage + metallic moiety.
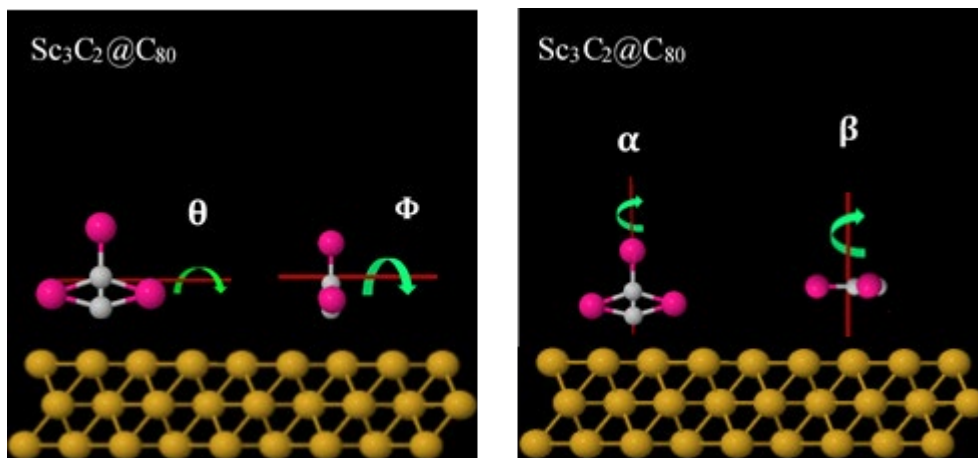
Figure S11. Illustration of how the four rotation axes θ, Φ, α and β, pass through the metallic moiety.

In what follows, the same symbol (e.g. θ) is used to label both the rotation axis and the angle of rotation about the axis.

5.3. Distance between the metallic moiety and the Au-substrate

Here, we calculate the distance between the metallic moiety and the gold substrate, while we rotate the metallic moiety on the substrate as shown in Figs S10 and S11. The distance d is defined to be the smallest vertical distance between the top-most plane of the Au substrate and the closest metal atom. Fig. S12 illustrates how d varies during rotations about the four different rotation axes θ, Φ, α and β, and shows that rotation about θ causes the largest distance variation (black and grey curves), followed by rotation about Φ (brown and yellow curves). In contrast, by symmetry, rotation about α and β causes no change in d (light and dark green or red and pink curves, respectively).

To quantify this variation, Table S2 shows the standard deviation σ of the distance d, associated with rotations about the four axes. This shows that the standard deviations σ follow the order $\sigma_\theta > \sigma_\Phi > \sigma_\alpha = \sigma_\beta$.
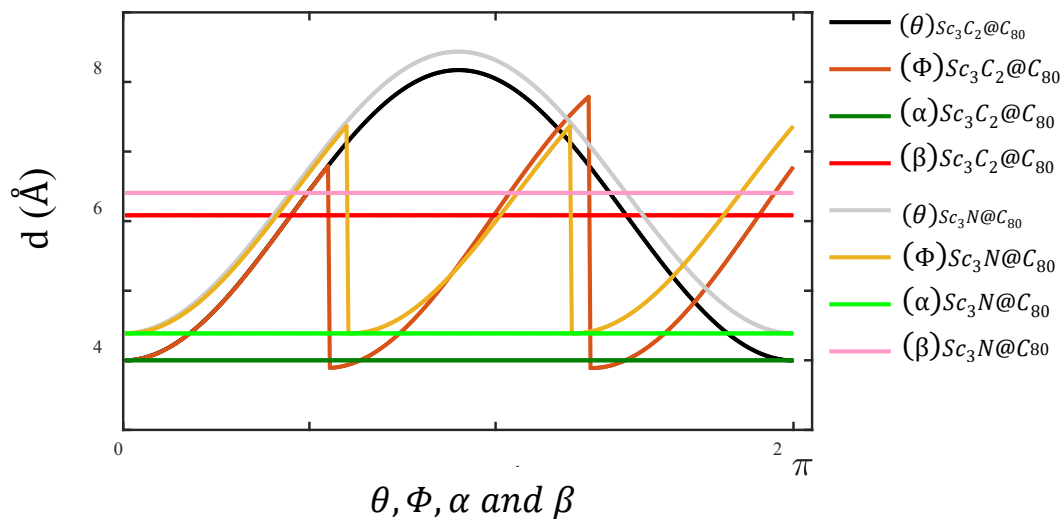
Figure S12. Distance variation between the metallic moiety and the gold substrate in four different rotation axes θ, Φ, α and β of $Sc_3C_2@C_{80}$, and $Sc_3N@C_{80}$ (*Note: $Sc_3N@C_{80}$ and $Er_3N@C_{80}$ have identical results, for clarity we present only $Sc_3N@C_{80}$ results*)

Table S2. Standard deviations σ of the distance d, associated with rotations about the four axes, for the three EMFs $Sc_3C_2@C_{80}$, $Sc_3N@C_{80}$ and $Er_3N@C_{80}$. In the latter case, the distance d is defined to be the smallest vertical distance between the top-most plane of the Au substrate and the closest Er atom.

EMF	σ_d (Å)			
	σ_θ	σ_Φ	σ_α	σ_β
$Sc_3C_2@C_{80}$	1.47	1.09	0	0
$Sc_3N@C_{80}$	1.43	0.95	0	0
$Er_3N@C_{80}$	1.43	0.95	0	0

5.4. Binding energies of EMFs on a gold surface

To calculate the optimum binding distance for EMFs between the gold (111) surface and the EMF, we use DFT, combined with the counterpoise method, which removes basis set superposition errors (BSSE). As shown by the example of $Sc_3C_2@C_{80}$ in Figure S13, the distance z is defined as the distance between the Au surface and the nearest C atom of the C_{80} cage (see the white double-arrow on the right panel of Figure S13).

The ground state energy of the total system is calculated using SIESTA[5] and is denoted E_{AB}^{AB}. Here the gold leads consist of 3 layers of 25 atoms. The $Sc_3C_2@C_{80}$ molecule is defined as monomer A and the gold electrodes as monomer B. The binding energy of each molecule is then calculated in a fixed basis, which is achieved through the use of ghost atoms in SIESTA. Hence the energy of the isolated $Sc_3C_2@C_{80}$ in the presence of the fixed basis is defined as E_A^{AB} and for the isolated gold is E_B^{AB}. The energy difference ($\Delta(z)$) between the isolated entities and their total energy when placed a distance z apart is then calculated using the following equation:

$$\text{Energy difference } = \Delta(z) = E_{AB}^{AB}(z) - E_A^{AB} - E_B^{AB} \tag{S1}$$

As shown by the Figure S13, the equilibrium distance for $Sc_3C_2@C_{80}$, corresponding to the minimum energy difference, is found to be approximately 2.5 Å, which is comparable with a value of 2.4 Å reported in Ref. [3].
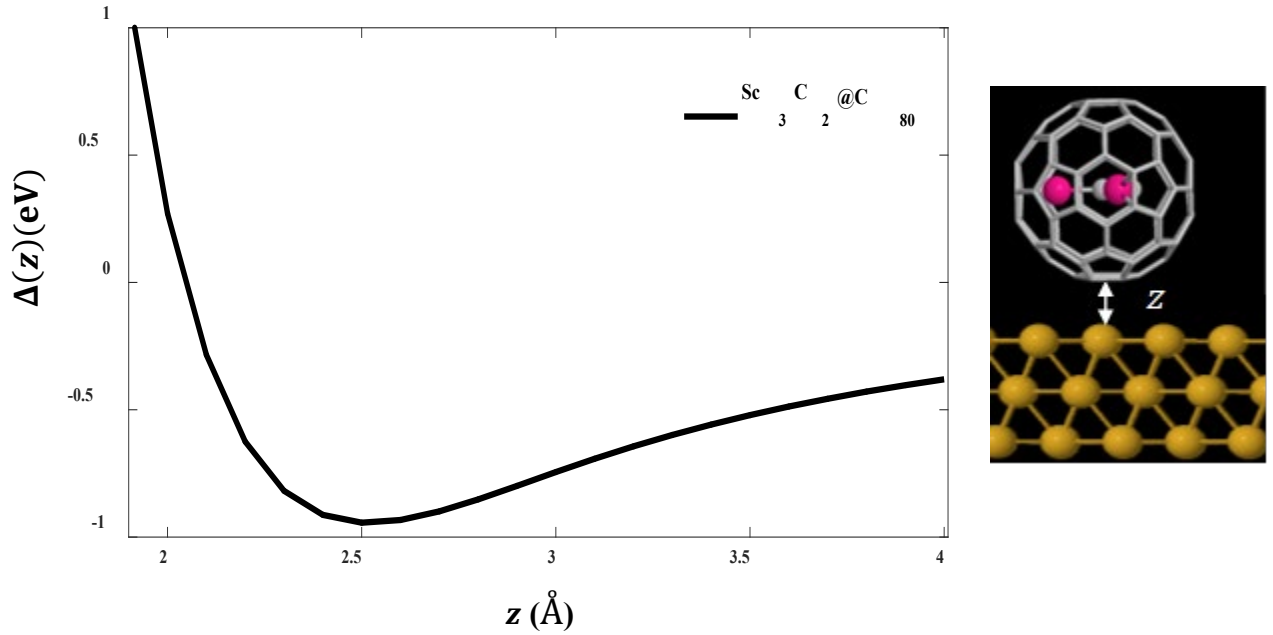

Figure S13. $Sc_3C_2@C_{80}$ on a gold surface (Right panel). Energy difference of $Sc_3C_2@C_{80}$/gold complex as a function of molecule-gold distance. The equilibrium distance corresponding to the energy minimum is found to be approximately 2.5 Å (Left panel).

5.5. Gas phase energy barriers to rotation for Sc₃C₂, Sc₃N and Er₃N within a I_h-C₈₀ cage

In this section, the metallic moieties Sc_3C_2, Sc_3N or Er_3N are rotated about horizontal axes θ and Φ and about a vertical axis α using equation (S2) as shown in Figure S14. Following equation (S1), the angle-dependent energy differences $\Delta(\theta)$, $\Delta(\Phi)$ and $\Delta(\alpha)$ are defined to be

$$\Delta(\theta) = E_{AB}^{AB}(\theta) - E_A^{AB} - E_B^{AB}$$

$$\Delta(\Phi) = E_{AB}^{AB}(\Phi) - E_A^{AB} - E_B^{AB} \qquad\qquad (S2)$$

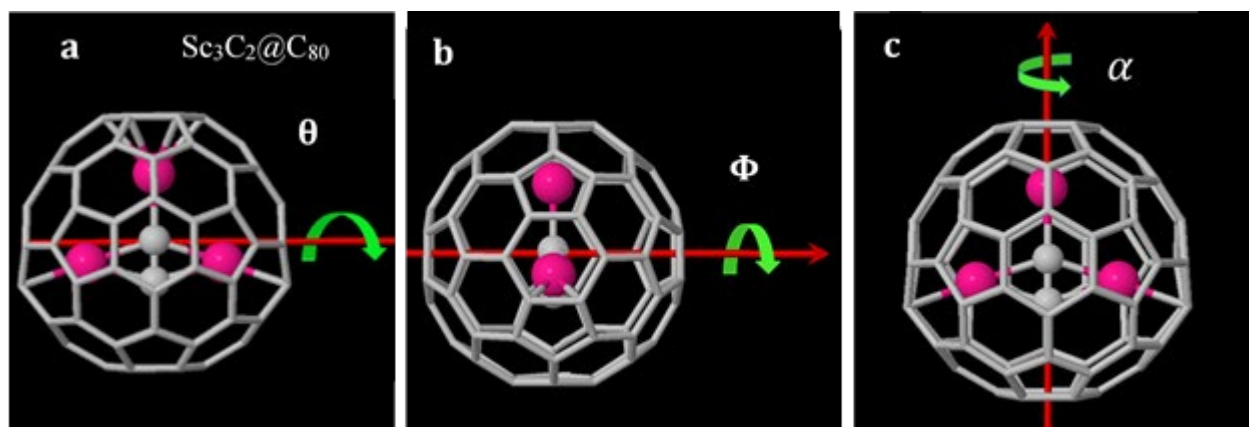$$\Delta(\alpha) = E_{AB}^{AB}(\alpha) - E_A^{AB} - E_B^{AB}$$

Figure S14. (a): Horizontal rotation axis used to compute $\Delta(\theta)$, (b): Horizontal rotation axis used to compute $\Delta(\Phi)$, (c): Vertical rotation axis used to compute $\Delta(\alpha)$, (Sc₃C₂@C₈₀ shown here as an example).

Figure S15 shows the gas-phase energy differences $\Delta(\theta)$ of Sc₃C₂@C₈₀, Sc₃N@C₈₀ and Er₃N@C₈₀ EMFs as a function of the rotation angle θ of the Sc₃C₂, Sc₃N and Er₃N inside the cages. This shows that the energy barrier to rotation about this horizontal axis is approximately $400, 300$ and 130 meV respectively, and that the Sc₃C₂, Sc₃N and Er₃N within the fullerene cage have preferred orientations θ of approximately $0°$, $190°$ and $360°$. The energy barrier to rotation Φ is $350, 250$ and 100 meV respectively, and therefore the moieties Sc₃C₂, Sc₃N, Er₃N have preferred orientations of $\Phi \approx (0°, 110°, 180°, 210°, 270°$ and $360°)$, $(10°, 95°, 200°, 280°$ and $340°)$ and $(0°, 120°, 250°$ and $350°)$. The energy barrier to rotation α is $300, 150$ and 60 meV respectively, and therefore the moieties Sc₃C₂, Sc₃N, Er₃N have preferred orientations of $\alpha \approx (0°, 75°, 160°, 240°$ and $320°)$, $(0°, 75°, 100°, 150°, 200°$ $250°, 300°$ and $350°)$ and $(0°, 80°, 150°, 225°, 320°$ and $360°)$. It is clear then that the energy barriers follow the

order $\theta > \Phi > \alpha$ for $Sc_3C_2@C_{80}$, $Sc_3N@C_{80}$ and $Er_3N@C_{80}$ EMFs. Similarly, the energy barriers follow the order $Sc_3C_2@C_{80} > Sc_3N@C_{80} > Er_3N@C_{80}$, These results are summarised in Table S3 and Table 2 in the main paper.
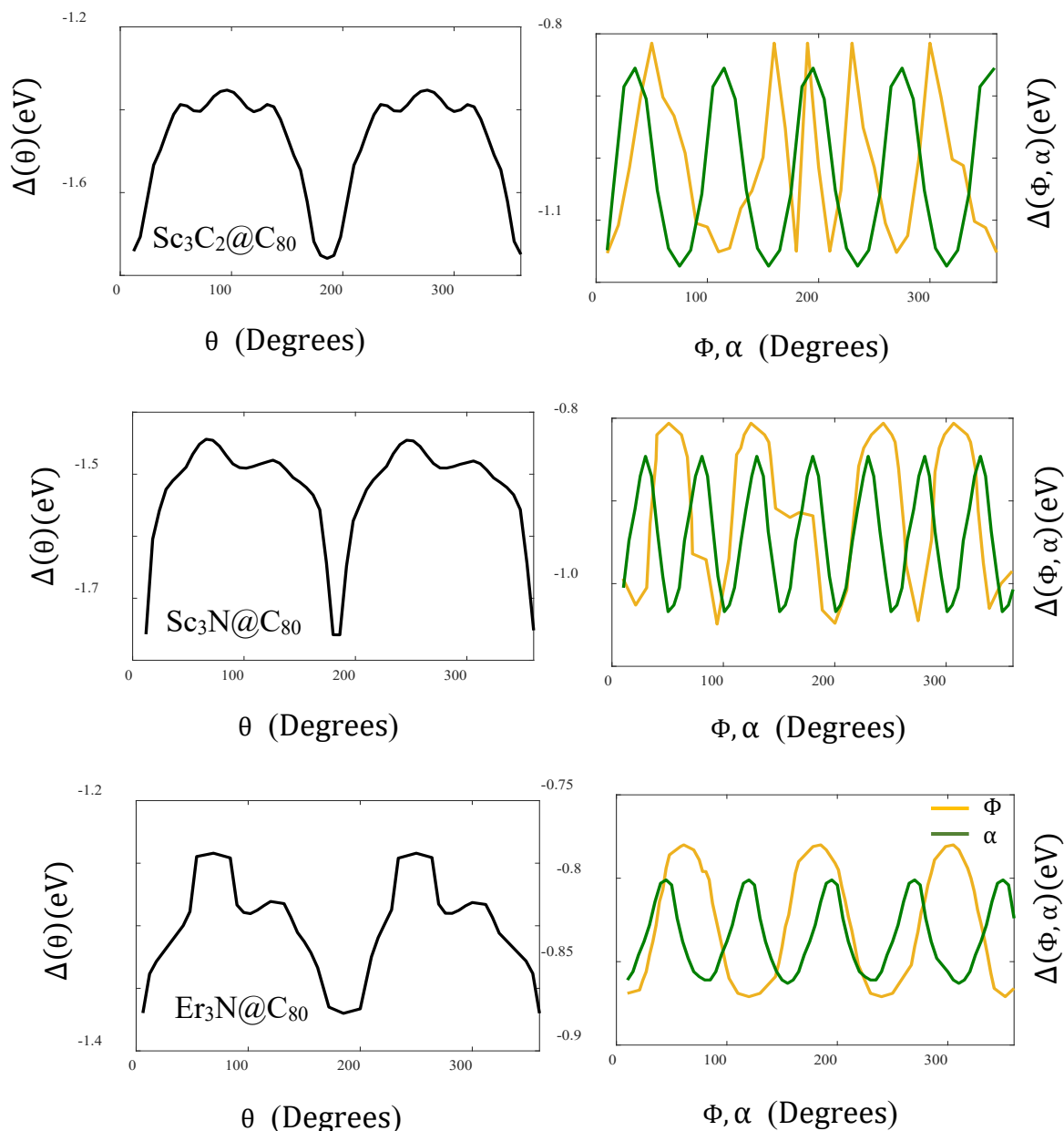

Figure S15. Left panels: The energy difference $\Delta(\theta)$ as a function of rotation angle θ of Sc_3C_2, Sc_3N and Sc_3N within the fixed I_h-C_{80} cage. Right panels: The energy differecne $\Delta(\Phi, \alpha)$ as a function of rotation angles Φ and α (yellow and green respectively), of Sc_3C_2, Sc_3N and Sc_3N within the fixed I_h-C_{80} cage. The energy barriers $\Delta E(\theta)$ to rotation about θ (obtained from the difference between the maxima and minima of $\Delta(\theta)$) are $400, 300$ and 130 meV respectively, and the moieties Sc_3C_2, Sc_3N, Er_3N have preferred orientations of $\theta \approx 0°$, $190°$ and $360°$, corresponding to the minima of $\Delta(\theta)$. The energy barriers $\Delta E(\Phi)$ to rotation about Φ are $350, 250$ and 100 meV respectively, and therefore the moieties Sc_3C_2, Sc_3N, Er_3N

have preferred orientations of $\Phi \approx$ (0°, 110°, 180°, 210°, 270° and 360°), (10°, 95°, 200°, 280° and 340°) and (0°, 120°, 250° and 350°). The energy barriers to rotation about α are 300, 150 and 60 meV respectively, and therefore the moieties Sc_3C_2, Sc_3N, Er_3N have preferred orientations of $\alpha \approx$ (0°, 75°, 160°, 240° and 320°), (0°, 75°, 100°, 150°, 200° 250°, 300° and 350°) and (0°, 80°, 150°, 225°, 320°and 360°). $Sc_3C_2@C_{80}$, $Sc_3N@C_{80}$ and $Er_3N@C_{80}$ top to bottom.

Table S3. Gas phase energy barriers $\Delta E(\theta)$, $\Delta E(\Phi)$, $\Delta E(\alpha)$ associated with rotations about θ, Φ, α of Sc_3C_2, Sc_3N and Er_3N within the fixed I_h-C_{80} cage, along with the preferred orientations angles for the three rotation axes.

EMF	$\Delta E(\theta)$ (meV)	Preferred orientations (θ)	$\Delta E(\Phi)$ (meV)	Preferred orientations (Φ)	$\Delta E(\alpha)$ (meV)	Preferred orientations (α)
$Sc_3C_2@C_{80}$	400	0°, 190° and 360°	350	0°, 110°, 180°, 210°, 270° and 360°	300	0°, 75°, 160°, 240° and 320°
$Sc_3N@C_{80}$	300	0°, 190° and 360°	250	10°, 95°, 200°, 280° and 340°	150	0°, 75°, 100°, 150°, 200° 250°, 300° and 350°
$Er_3N@C_{80}$	130	0°, 190° and 360°	100	0°, 120°, 250° and 350°	60	0°, 80°, 150°, 225°, 320°and 360°

Table S3 shows the energy barrier $\Delta E(\theta)$ for Er_3N inside the C_{80} cage is of order 130 meV, which means that the Er_3N cluster rotates more easily than the scandium-based moieties, Sc_3N and Sc_3C_2. Table S3 also shows that the barrier to rotation about a vertical axis $\Delta E(\alpha)$ is even lower, at approximately 60 meV. Figure S16 shows a comparison between the Er_3N and Sc_3C_2 moieties.
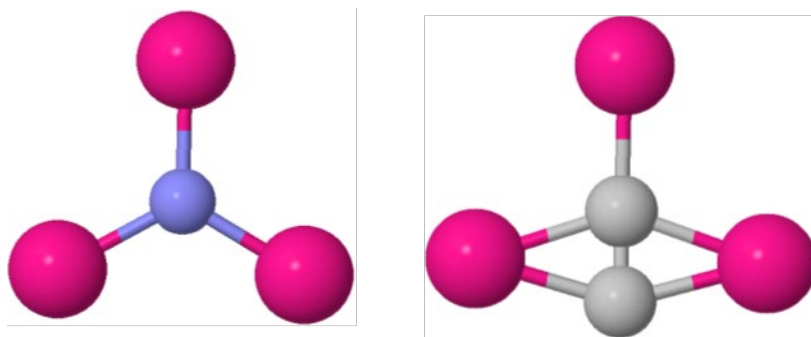

Figure S16. Geometries of the symmetric Er_3N and Sc_3N (left panel) and asymmetric Sc_3C_2 (right panel).

5.6. Energy barriers to rotation for endohedral fullerenes on a gold (111) surface

Having discussed barriers to rotation in the gas phase, we now calculate the energy $\Delta(\theta)$ when the whole EMF (cage plus metallic moiety) is rotated in the vicinity of a gold (111) surface, at various distances z relative to the surface. As an example, the rotation axis θ is shown in Figure S17 along with the definition of the distance z of the cage relative to the Au surface.
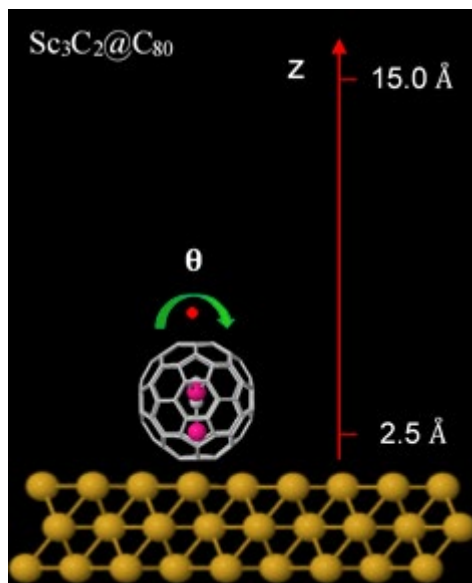

Figure S17. Illustration of the rotation axis θ and the Au-C_{80} distance (z) of $Sc_3C_2@C_{80}$ used to compute the results in Figures S18 and S19.

For each of $Sc_3N@C_{80}$, $Sc_3C_2@C_{80}$ and $Er_3N@C_{80}$, Figure S18 shows the energy $\Delta(\theta)$ obtained at different Au-C_{80} distances z, starting from the optimum distance $z = 2.5$ Å. At each distance z, $\Delta(\theta)$ is computed for values of θ ranging from 0 to 2π. At the optimum value z, the three black curves show that $Er_3N@C_{80}$ possesses the smallest rotation barrier ($\Delta E(\theta) = 0.1$ eV), whereas $Sc_3C_2@C_{80}$ and $Sc_3N@C_{80}$ possess energy barriers to rotation of $\Delta E(\theta) = 0.6$ eV and 0.3 eV, respectively. All those barriers decrease with increasing distance z, until they vanish at large z (which is approximately equivalent to the gas phase of the whole EMF). The three green curves in Figure S18 show the corresponding energies obtained by rotating the metallic moieties alone in the vicinity of a gold surface in the absence of the C_{80} cage, at $z = 2.5$ Å. This shows that for bare Sc_3C_2 and Sc_3N (i.e. in the absence of the cage) the rotational energy barriers are slightly smaller and are negligible for the bare Er_3N.
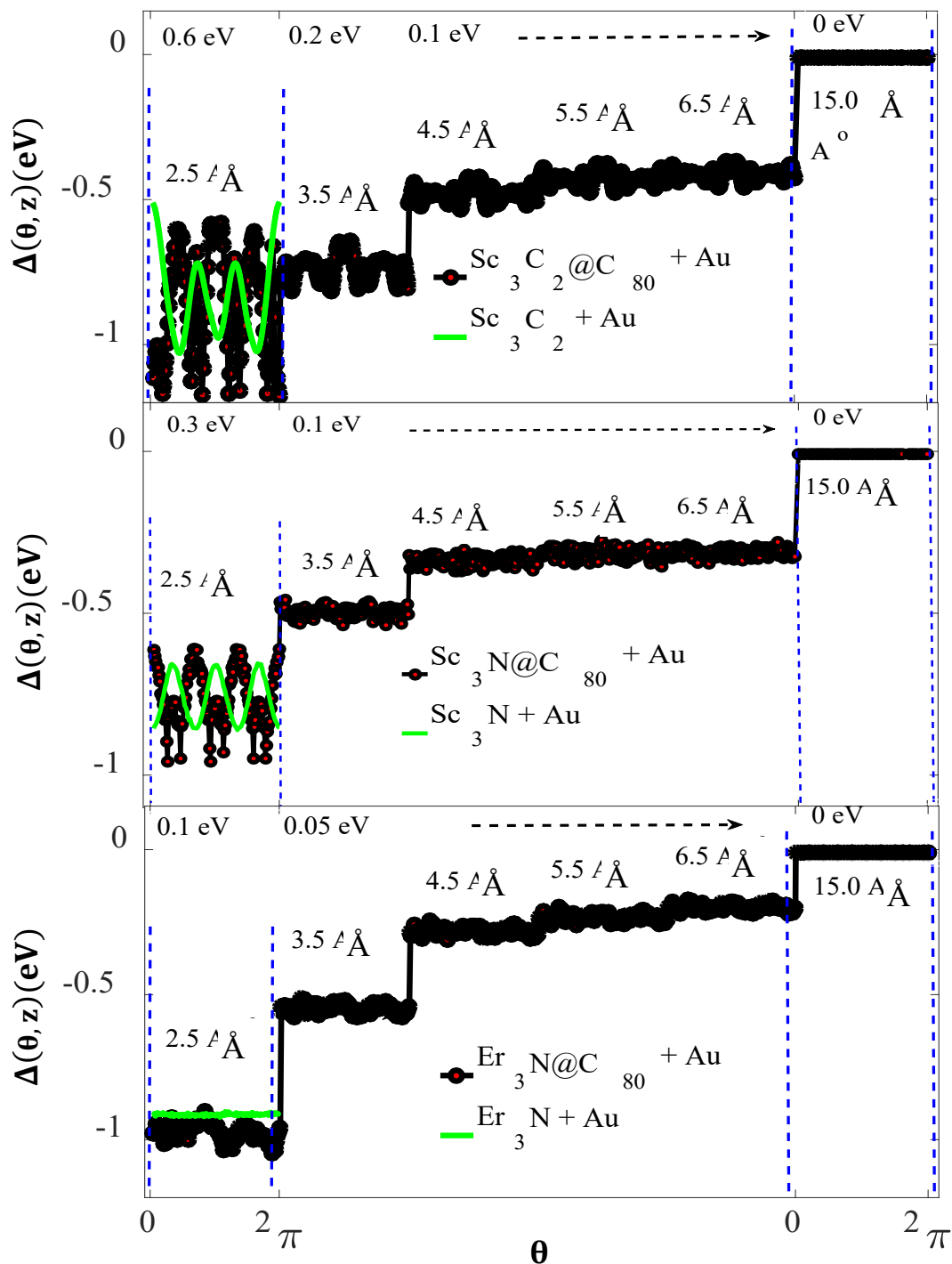
Figure S18. Rotational energy barriers of the three EMFs on a gold surface ($Sc_3C_2@C_{80}$, $Sc_3N@C_{80}$ and $Er_3N@C_{80}$, respectively) computed at different distances z from the surface, for the rotation axis θ. The energy barriers to rotation are of the order 0.6, 0.3 and 0.1 eV at $z = 2.5$ Å and tend to zero for large z (black lines). The green curves show the energy barriers to rotation for the three bare metallic moieties near a gold surface, at $z = 2.5$ Å, in the absence of C_{80}.

In the above calculations, the whole EMF or just the bare metallic cluster were rotated in the vicinity of a gold substrate. As a separate check on the energy barriers, we now keep the cage at a fixed orientation and compute the energy $\Delta(\theta, z)$ versus z for rotation angles θ of the metallic cluster inside the cage, which correspond to the energy minima of Table S3. For Sc_3C_2, (Figure S19a) the four different angles used are $\theta = 0°, 90°, 180°, 270°$. For Sc_3N (Figure S19b), the three different angles are $\theta = 0°, 90°, 180°$. The differences between the energy minima of these plots match the results of the middle panel of Figure S18. These results show that Sc_3C_2 possesses the highest barrier, in agreement with the top panel of Figure S18. For Er_3N, (Figure S19c) three different angles are used $\theta = 0°, 90°, 180°$. This shows that the energy barrier is relatively small and in agreement with the bottom panel of Figure S18.
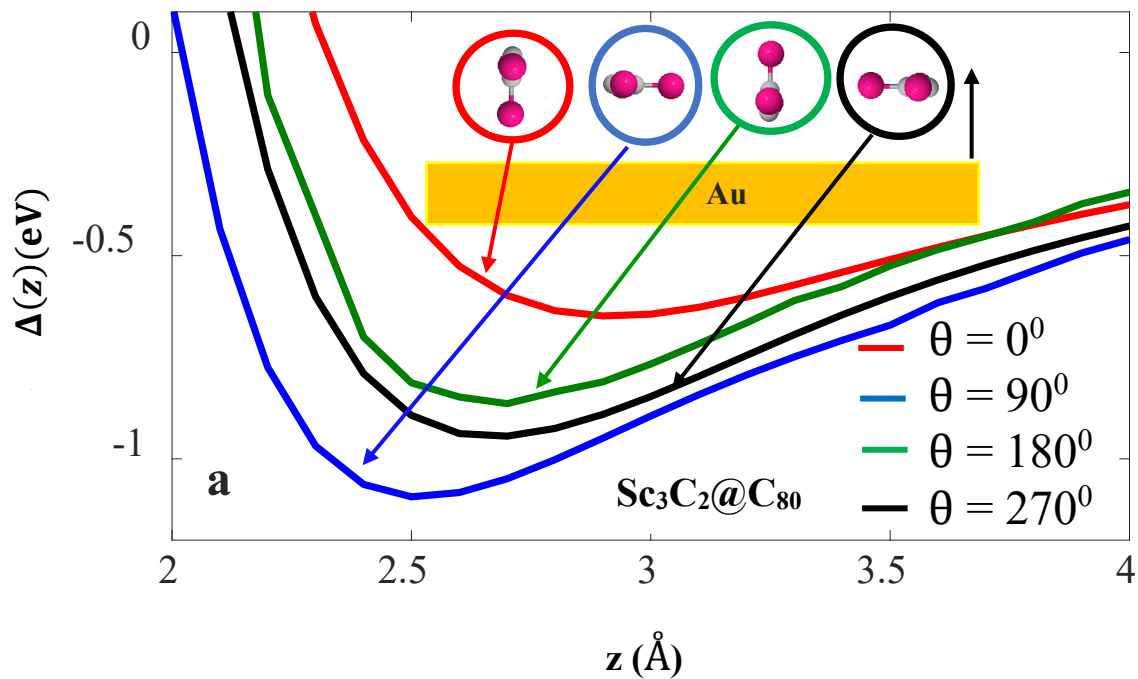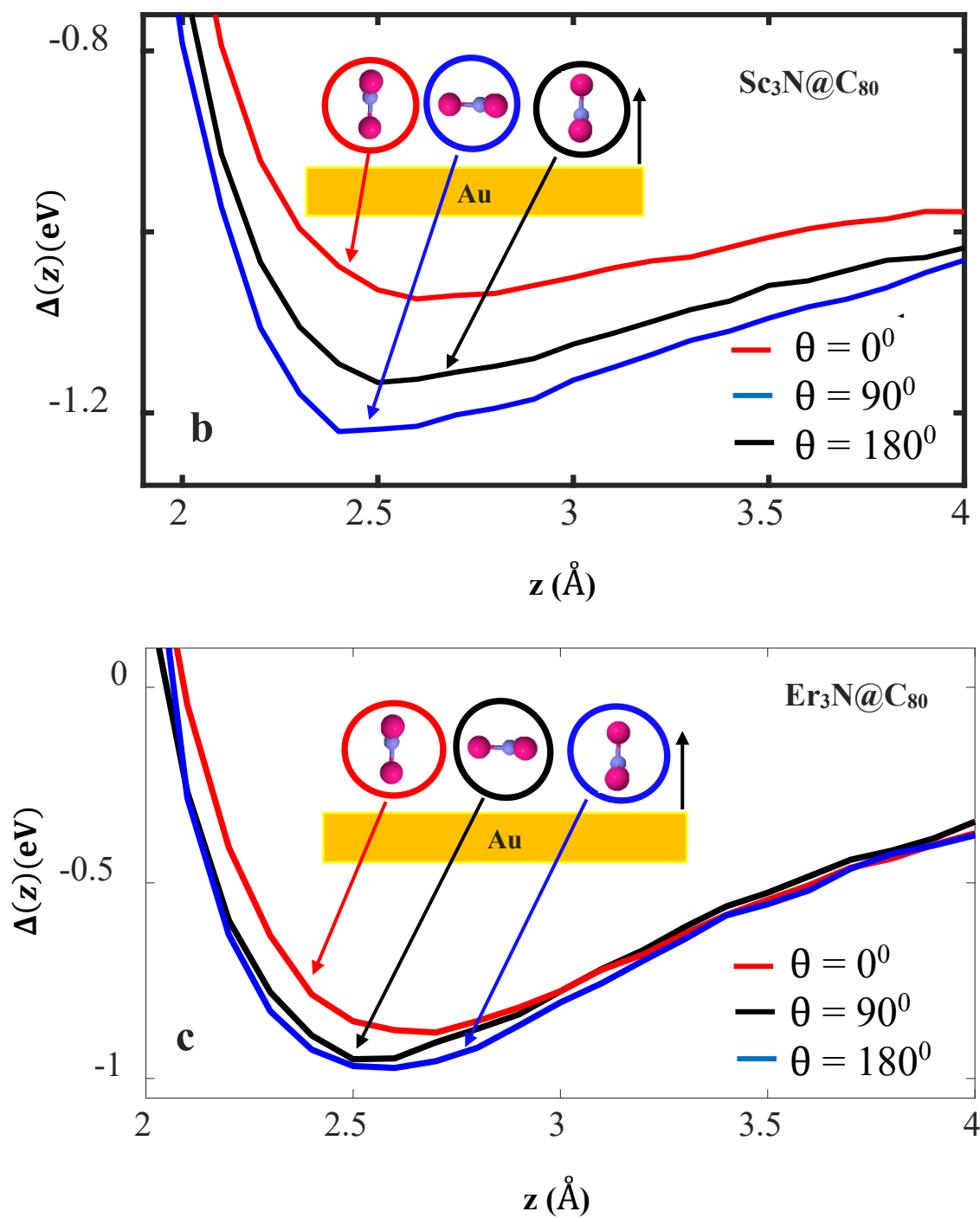
Figure S19. The energy difference $\Delta(z)$ as a function of the distance z for different orientations of the metallic clusters inside the cage **a, b** and **c** correspond to $Sc_3C_2@C_{80}$, $Sc_3N@C_{80}$, and $Er_3N@C_{80}$, respectively.

We now repeat the calculations shown in Figure. S18 using the different rotation axes θ, Φ, α and β on the Au substrate as shown in Figure S20. We calculate the energies $\Delta(\theta), \Delta(\Phi), \Delta(\alpha), \Delta(\beta)$ when the whole EMF (cage plus metallic moiety) is rotated in the vicinity of a gold (111) surface.
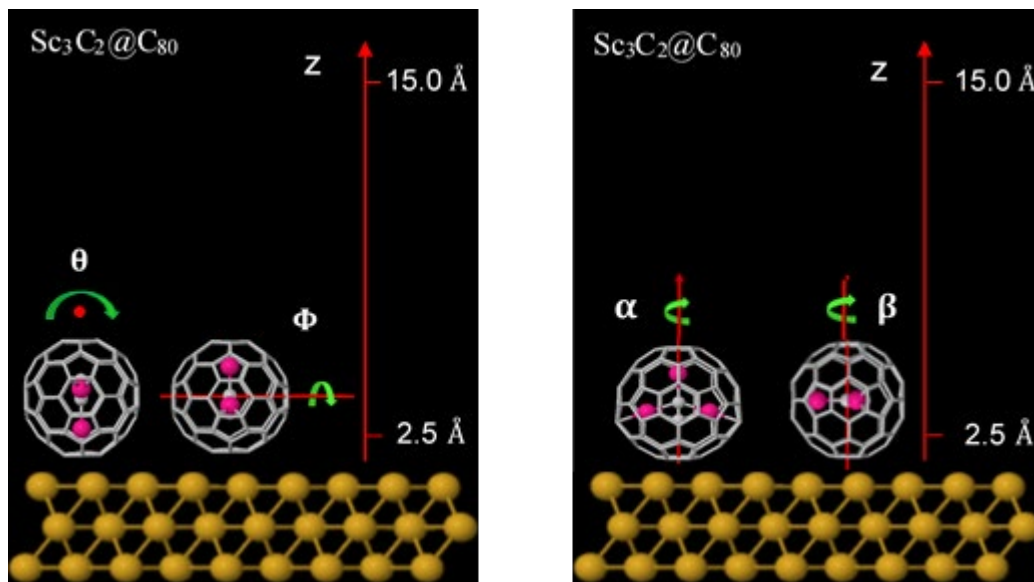

Figure S20. Illustration of the rotation axes and the Au-C_{80} distance (z), used to compute the results in Figure S21.

Figure S21 shows the binding energy is rather sensitive to rotation about the θ and Φ axes and are relatively insensitive to rotation about axes α and β. Consequently the energy barriers to rotation follow the order $\Delta E(\theta) > \Delta E(\Phi) > \Delta E(\alpha) > \Delta E(\beta)$. This ordering illustrates a rather intuitive structure-function relation, because it is correlated with the standard deviations σ of Table S2, which follow the order $\sigma_\theta > \sigma_\Phi > \sigma_\alpha = \sigma_\beta$. This shows that large variations in the distance between the metal atom and the substrate lead to large variations in the binding energy and larger energy barriers to rotation, whereas the negligible variations in the distance associated with the α and β axes lead to much smaller energy barriers.
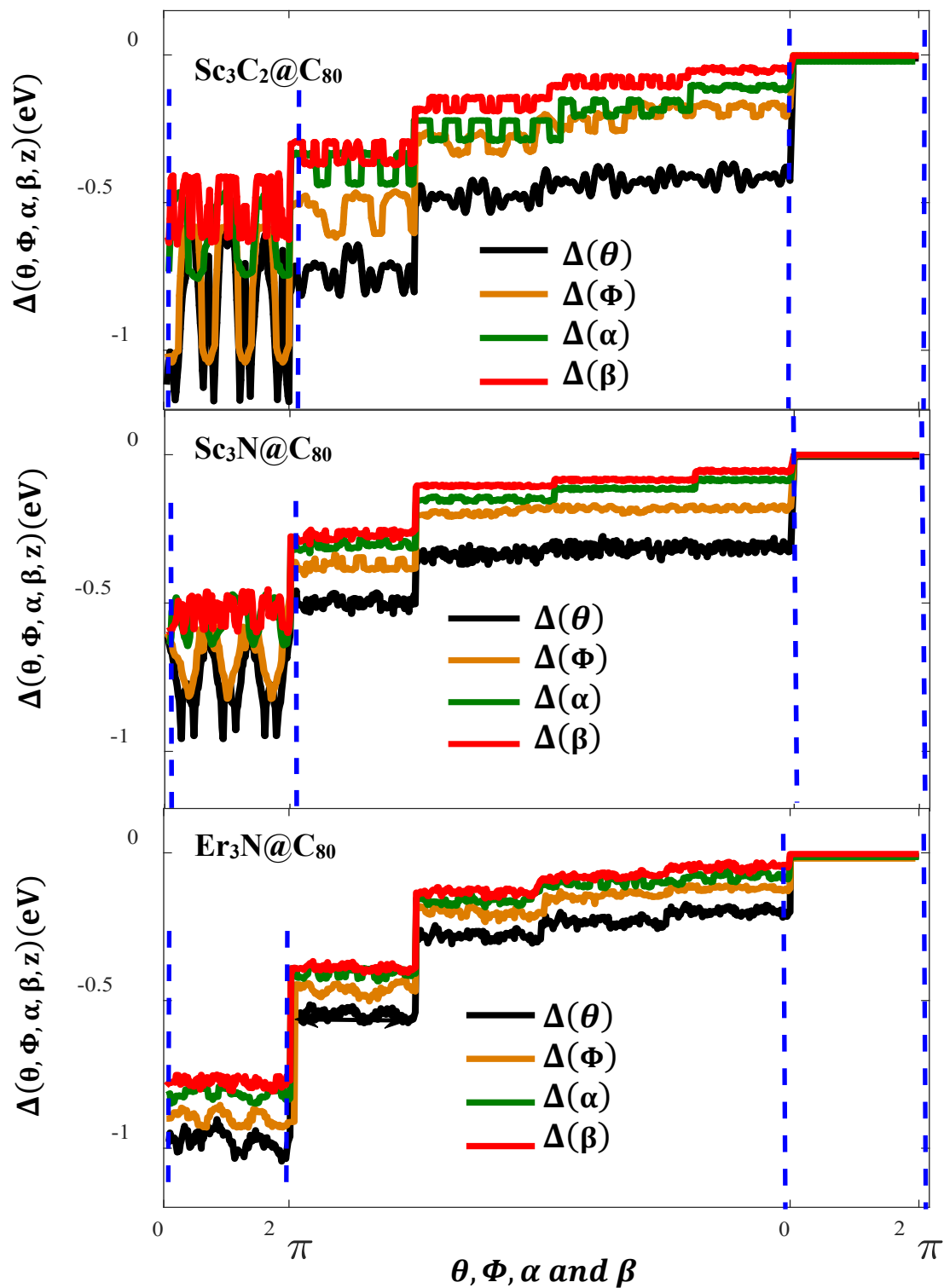
Figure S21. Rotational energy barriers of the three EMFs onto a gold surface ($Sc_3C_2@C_{80}$, $Sc_3N@C_{80}$, and $Er_3N@C_{80}$, respectively) as a function of rotation and distance to the surface in four rotational axes θ, Φ, α and β. The energy barrier to rotation (β-axes) is of the order of 0.25, 0.1 and 0.04 eV at $z = 2.5$ Å and tends to zero for large z (red lines); for the energy barrier to rotation (θ, Φ, α and β axes) see Figure S22.

5.7. Spin-dependent transport calculations for different rotation angles (θ) about a horizontal axis

Figure S22 shows the definition of the orientation angle of the $Sc_3C_2@C_{80}$ molecule from $\theta = 0^\circ$ to 90°. Figure S23 shows an example of the spin-dependent transmission coefficients *T(E)* for the optimum geometry (60°) shown in Figure S22. These reveal that the calculated transmission for spin-up ($T_{up}(E)$) and spin-down ($T_{down}(E)$) show that the resonance is split as expected due to the charge transfer from the metallic moiety to the cage, which positions the resonance close to the Fermi energy. The total transmission is then given by $\frac{T_{up}(E)+T_{down}(E)}{2}$ as shown in Figure S23.
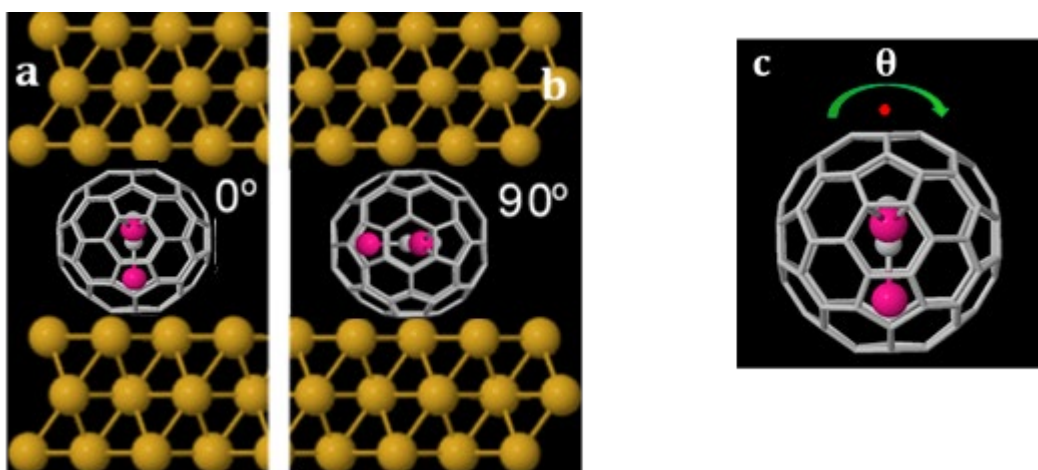

Figure S22. $Sc_3C_2@C_{80}$ between gold surfaces. The orientation of the $Sc_3C_2@C_{80}$ molecule with respect to the gold leads corresponds to the defined angle (**a**) $\theta = 0^\circ$, (**b**) $\theta = 90^\circ$. (**a** and **b**): a view in which the rotation axis is perpendicular to the plane of the paper, (**c**): The horizontal rotation axis θ.
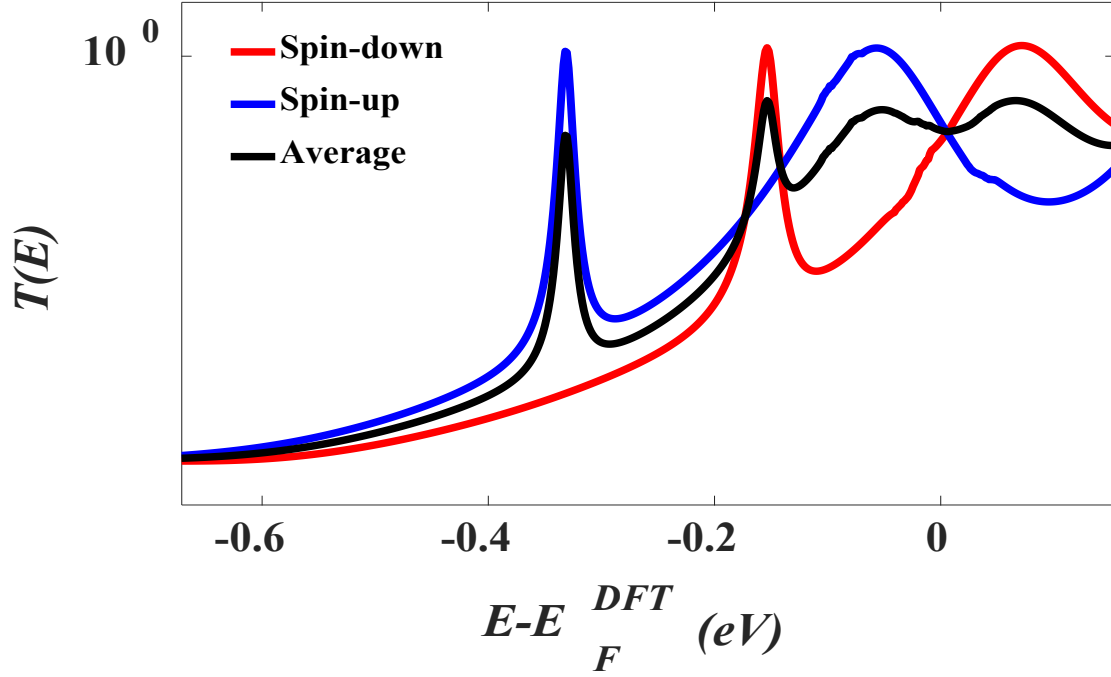
Figure S23. Spin-polarised transmission coefficients $T_{up}(E)$, $T_{down}(E)$ and $T(E) = \frac{T_{up}(E) + T_{down}(E)}{2}$, for the binding configuration of 60° orientation θ of $Sc_3C_2@C_{80}$ and z = 2.5 Å. The three curves represent the spin-up, spin-down and the average of them: blue, red and black curves, respectively.

Figure S24 shows the average transmission coefficients for different orientations of $Sc_3C_2@C_{80}$ (see Figure S22). Similarly, Figure S25 shows the average transmission coefficients for 60 different orientations of $Sc_3N@C_{80}$. In contrast, the transmission coefficient of C_{60} is spin-independent. By comparing Figures S24 and S25, one can notice the fluctuations in the $Sc_3C_2@C_{80}$ transmission curves are larger than those of the $Sc_3N@C_{80}$ curves.
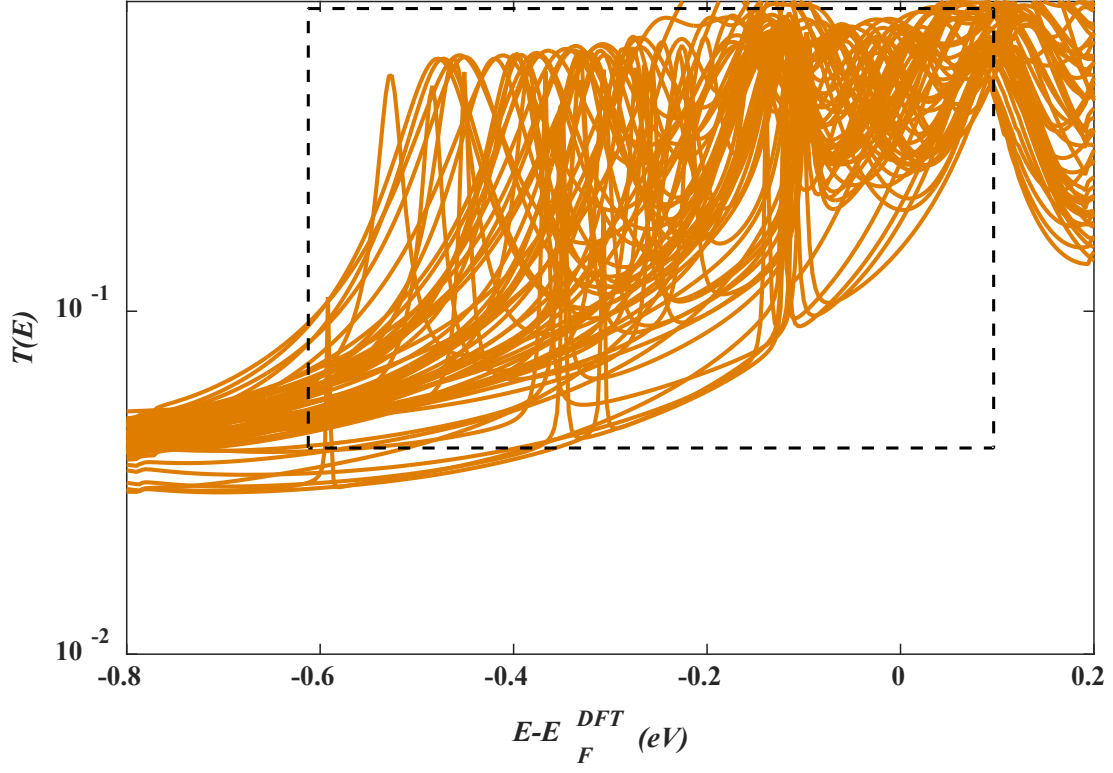
Figure S24. Spin-polarised transmission coefficients, $T(E) = \frac{T_{up}(E) + T_{down}(E)}{2}$, for the 60 binding configurations of different orientations θ for $Sc_3C_2@C_{80}$, and $z = 2.5$ Å.
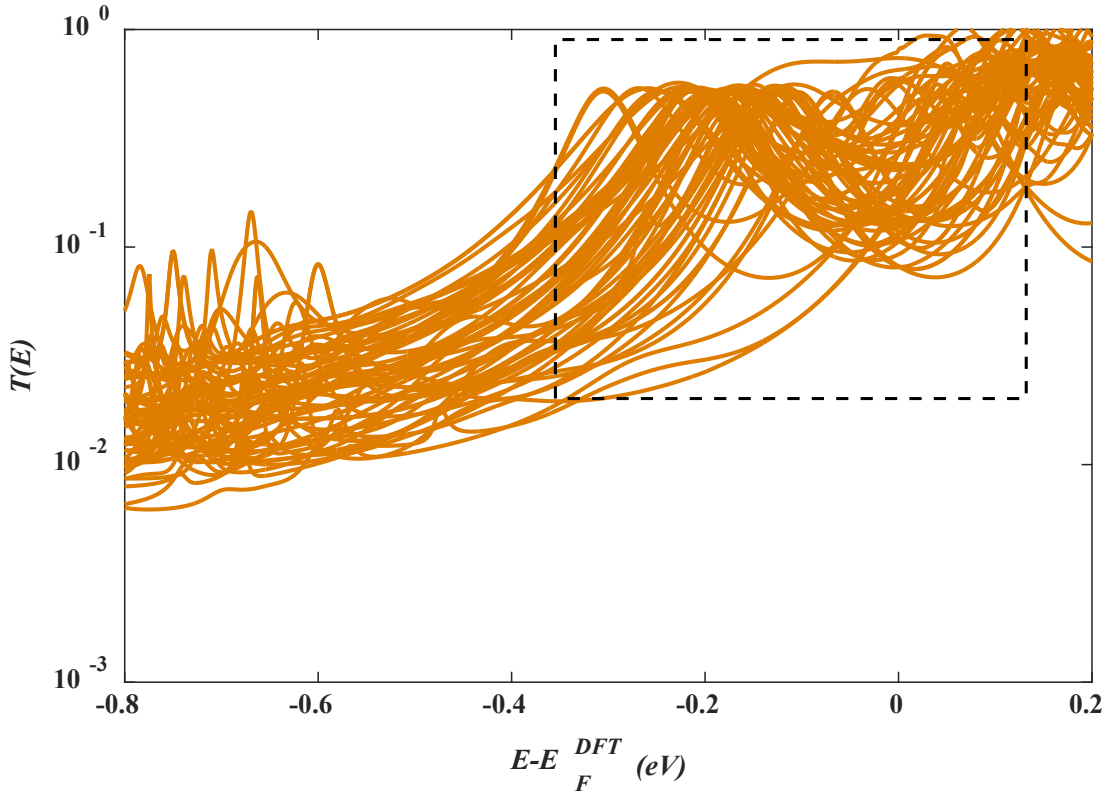
Figure S25. Spin-polarised transmission coefficients, $T(E) = \frac{T_{up}(E) + T_{down}(E)}{2}$, for the 60 binding configurations of different orientations θ for Sc$_3$N@C$_{80}$, and $z = 2.5$ Å.

5.8. Calculated thermopower as a function of orientation in the horizontal rotation axis (θ)

To calculate the thermopower of these molecular junctions, it is useful to introduce the non-normalised probability distribution $P(E)$ defined by

$$P(E) = -T(E)\frac{df(E)}{dE} \tag{S3}$$

where $f(E)$ is the Fermi-Dirac function and $T(E)$ is the transmission coefficients and whose moments L_i are denoted as follows

$$L_i = \int dE P(E)(E - E_F)^i \tag{S4}$$

where E_F is the Fermi energy. The Seebeck coefficient, S, is then given by

$$S(T) = -\frac{1}{eT}\frac{L_1}{L_0} \tag{S5}$$

where e is the electronic charge.

Note that in ref [75] of the main manuscript, equation (50), contains a typographical error and is not the formula evaluated by the Gollum code. The formula evaluated by Gollum is

$$S^e(T) = \frac{-1}{eT}\frac{L_1}{L_0}$$

where

$$L_i = \int dE P(E)(E - E_F)^i$$

and

$$P(E) = -T(E)\frac{df(E)}{dE}$$

In this expression, $T(E) = \frac{T_{up}(E) + T_{down}(E)}{2}$, where $T_{up}(E)$ and $T_{down}(E)$ are transmission coefficients for the separate spin channels and it is assumed that there is no spin-flip scattering.

This equation describes the linear response regime and is consistent with Onsager reciprocal relations.

Figures S26 and S27 show the average Seebeck coefficient S evaluated at room temperature for different orientation angles of θ for $Sc_3C_2@C_{80}$ and $Sc_3N@C_{80}$.

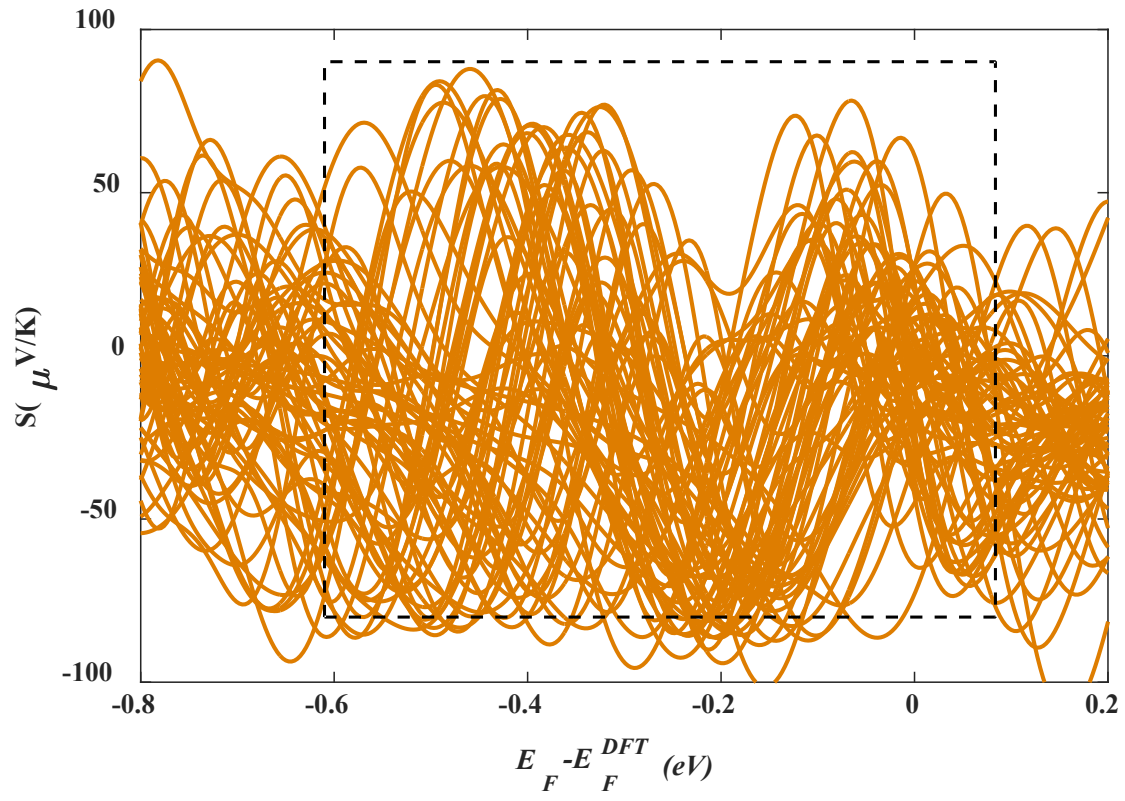**Figure S26.** Seebeck coefficient *S* as a function of Fermi energy at 60 different orientations angles θ of Sc$_3$C$_2$@C$_{80}$, for a tip-substrate distance of 2.5 Å.
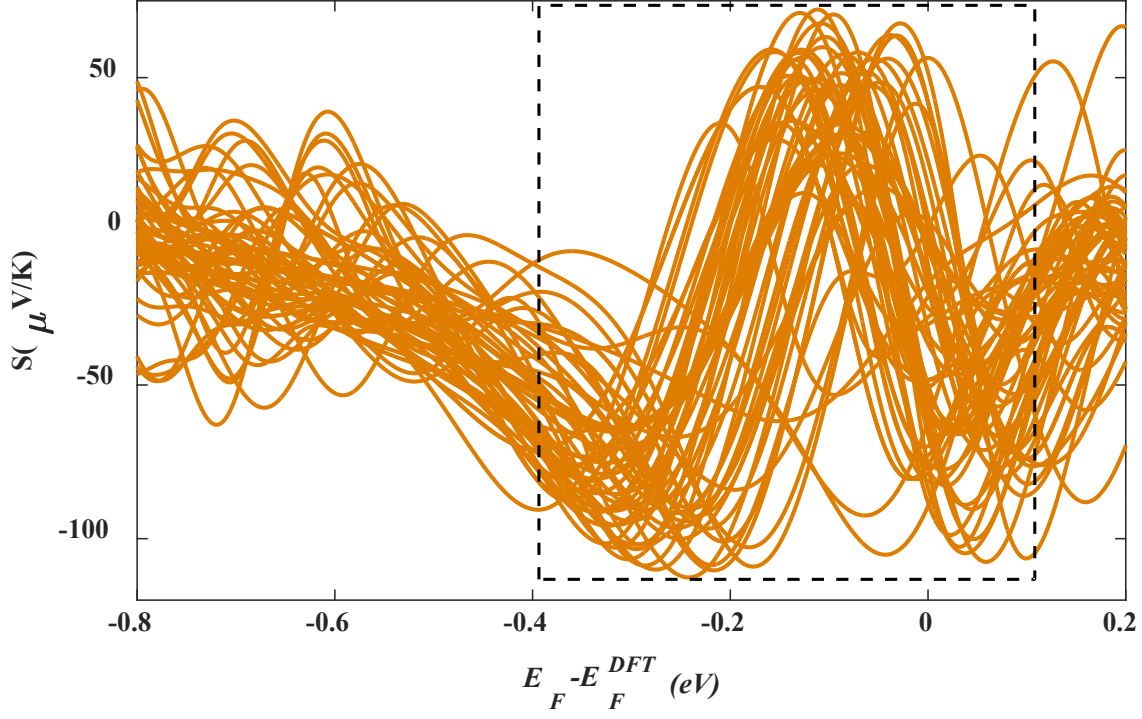
Figure S27. Seebeck coefficient *S* as a function of Fermi energy at 60 different orientations angles θ of Sc$_3$N@C$_{80}$. *S* versus Fermi energy at different orientation angles θ for a tip-substrate distance of 2.5 Å.

5.9. Spin-dependent transport calculations for different orientations (*Φ*) about a horizontal rotation axis

In this section, we repeat the calculations described in section 5.7, but using the horizontal rotation axis (*Φ*), as shown in Figure S28. As expected the fluctuations in the transmission coefficients are smaller when

the EMF rotates about the Φ axis, because the variation in the distance between the metallic part Sc_3C_2/ Sc_3N and the cage C_{80} is smaller compared to rotation in θ axis as shown in Figures. S29-S30.
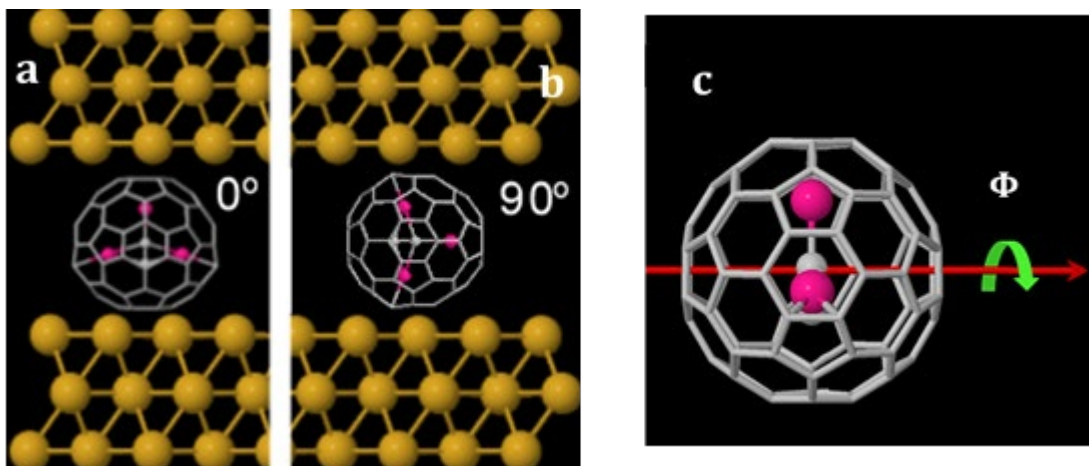

Figure S28. $Sc_3C_2@C_{80}$ between gold surfaces. (**a-b**): The orientation of the $Sc_3C_2@C_{80}$ molecule with respect to the gold leads. (**c**): The horizontal rotation axis Φ.

Figure S29. Spin-polarised transmission coefficients, $T(E) = \frac{T_{up}(E) + T_{down}(E)}{2}$, for the 60 binding configurations of different orientations Φ of $Sc_3C_2@C_{80}$, and $z = 2.5$ Å.
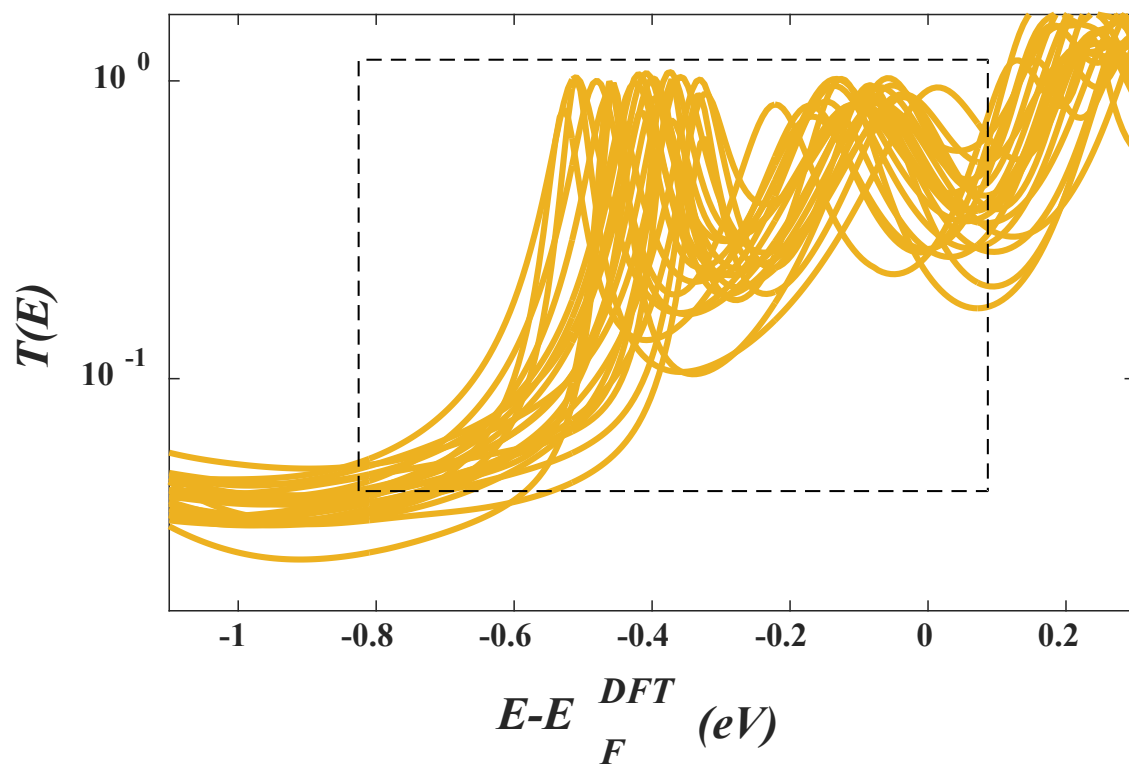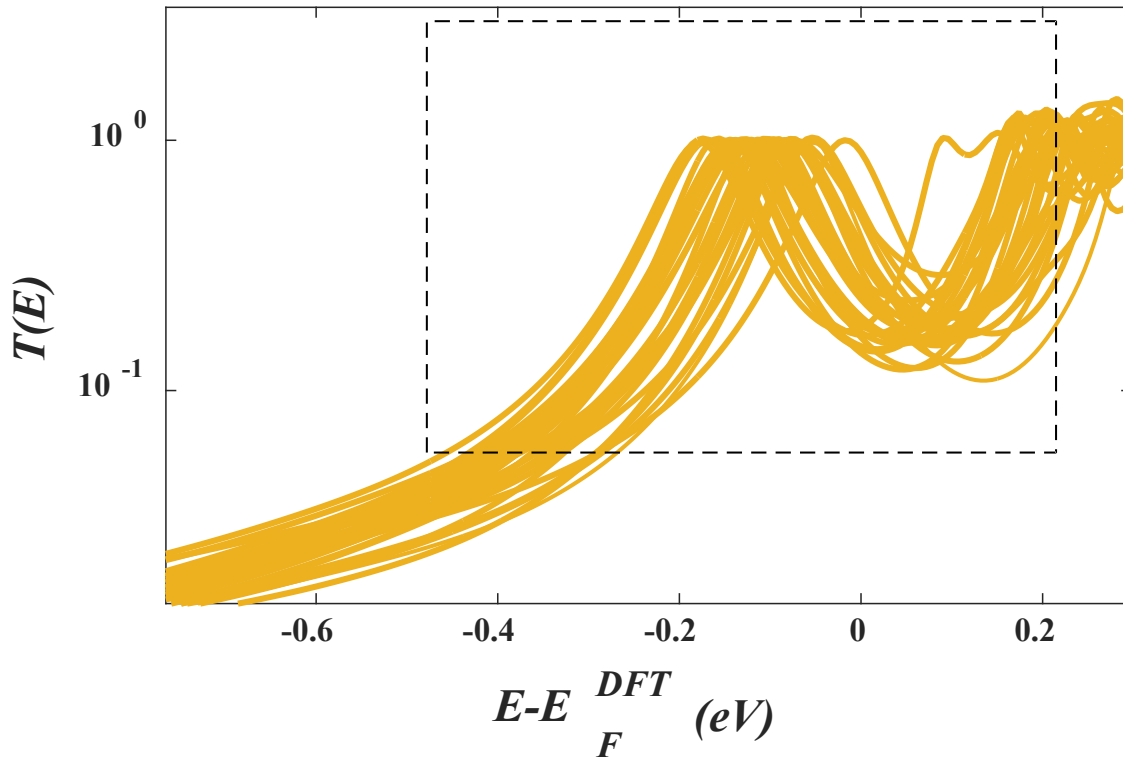
Figure S30. Spin-polarised transmission coefficients, $T(E) = \frac{T_{up}(E) + T_{down}(E)}{2}$, for the 60 binding configurations of different orientations Φ of $Sc_3N@C_{80}$, and $z = 2.5$ Å.

5.10. Calculated thermopower as a function of orientation in the horizontal rotation axis (Φ)

Figures S31 and S32 show the average Seebeck coefficient S evaluated at room temperature for different orientation angles of Φ for $Sc_3C_2@C_{80}$ and $Sc_3N@C_{80}$.
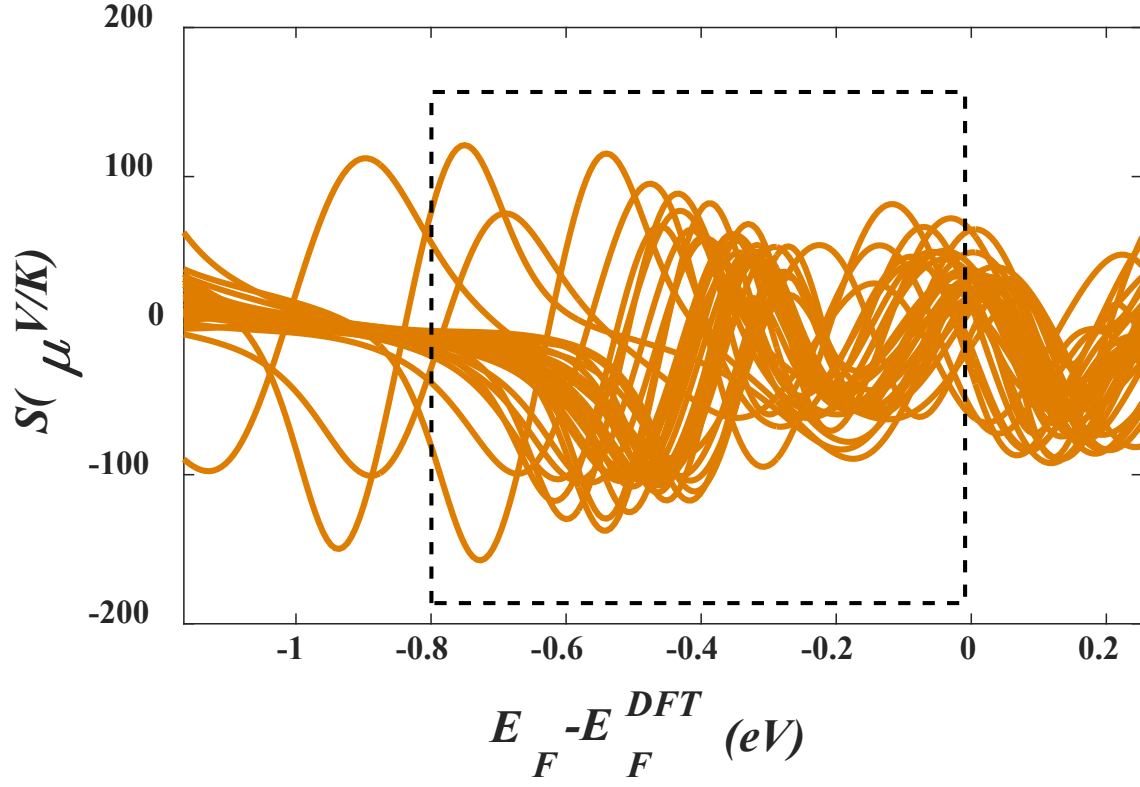
Figure S31. Seebeck coefficients S as a function of Fermi energy at 60 different orientation angles Φ of $Sc_3C_2@C_{80}$, for a tip-substrate distance of 2.5 Å.
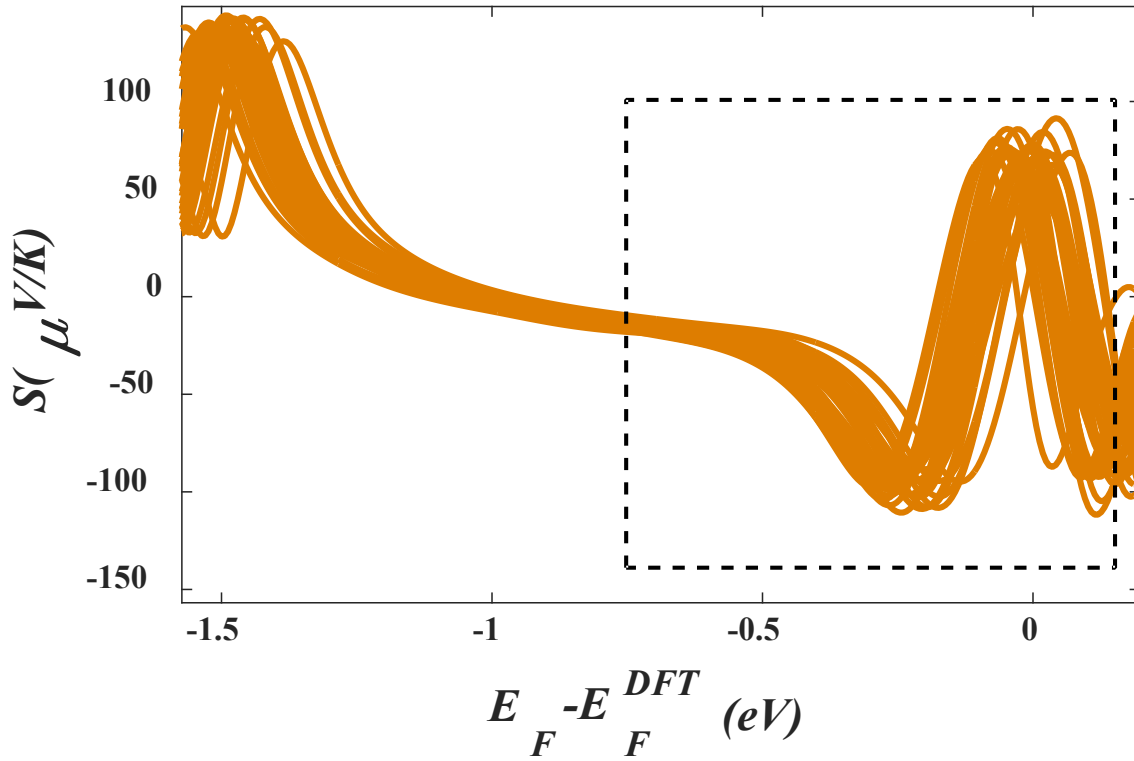
Figure S32. Seebeck coefficients S as a function of Fermi energy at 60 different orientation angles Φ of Sc$_3$N@C$_{80}$ for a tip-substrate distance of 2.5 Å.

5.11. Spin-dependent transport calculations in the vertical rotation axis (α)

In this section, we repeat the calculations described in section 5.7, using rotation angles about the vertical rotation axis (α), as shown in Figure S33. As expected, compared to the rotations about the θ axis, Figures S34 and S35 show that the fluctuations in the transmission coefficients are smaller when the EMF rotates about this vertical axis, because the rotation causes a smaller variation in the distance between the metallic part Sc$_3$C$_2$/Sc$_3$N and the cage C$_{80}$. Since the rotation in this axis (α), has small effect on the transmission coefficient curves, Figures S36 and S37 show that the Seebeck coefficient S does not show strong fluctuations (see next section).
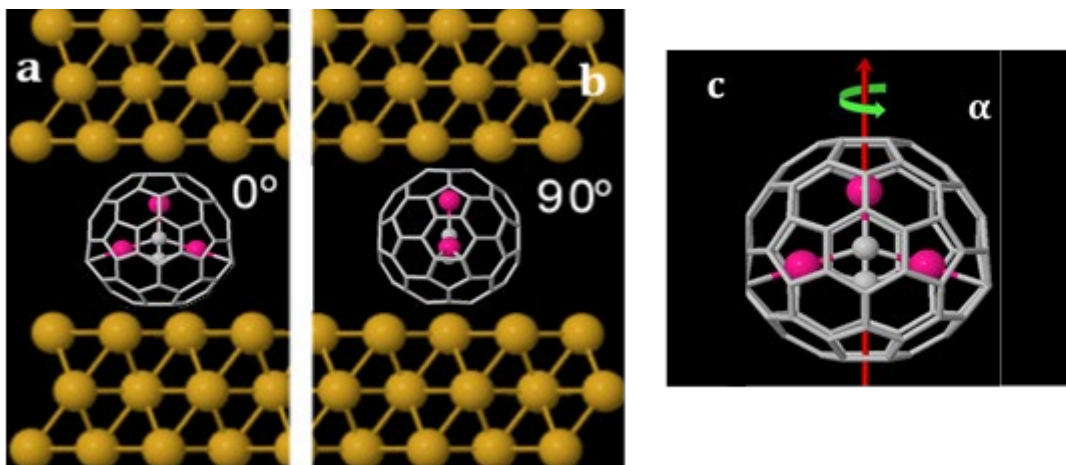
Figure S33. $Sc_3C_2@C_{80}$ between gold surfaces. (**a-b**): The orientation of the $Sc_3C_2@C_{80}$ molecule with respect to the gold leads. (**c**): The vertical rotation axis α.

Figure S34. Spin-polarised transmission coefficients, $T(E) = \frac{T_{up}(E) + T_{down}(E)}{2}$, for the 60 binding configurations of different orientations α of $Sc_3C_2@C_{80}$, and $z = 2.5$ Å.
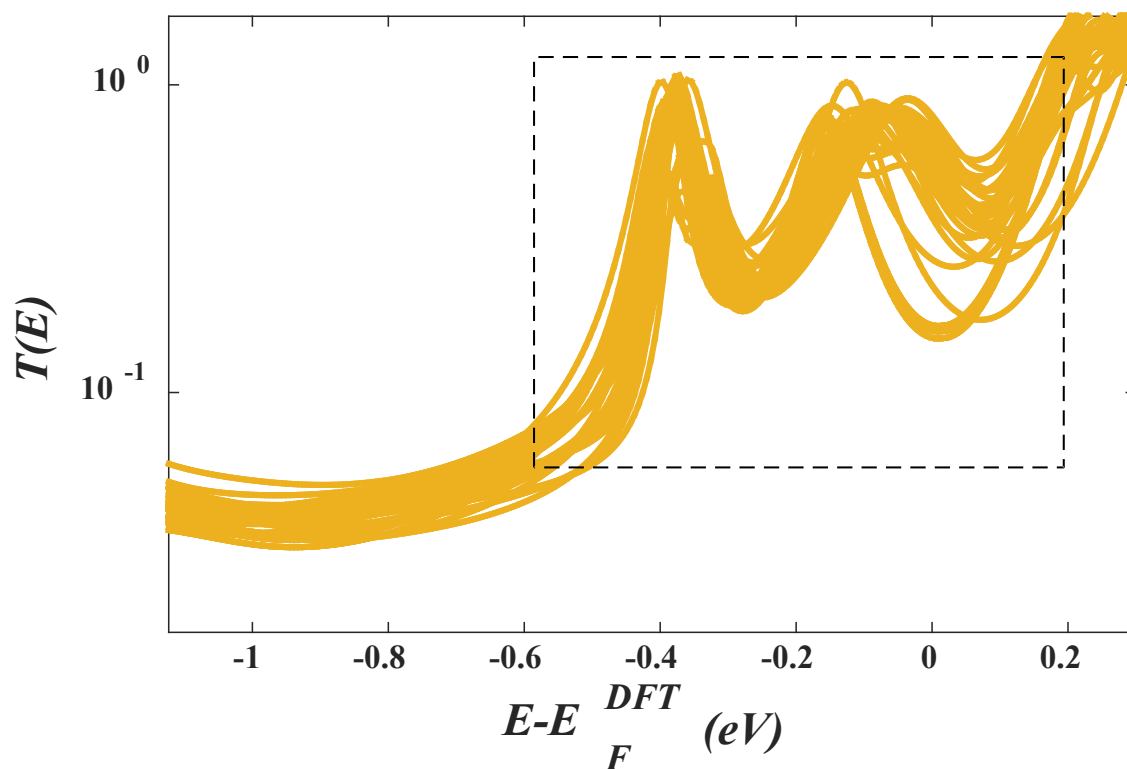
Figure S35. Spin-polarised transmission coefficients, $T(E) = \frac{T_{up}(E) + T_{down}(E)}{2}$, for the 60 binding configurations of different orientations α of $Sc_3N@C_{80}$, and $z = 2.5$ Å.

5.12. Calculated thermopower as a function of orientation in the vertical rotation axis (α)

Figures S36 and S37 show the average Seebeck coefficient S evaluated at room temperature for different orientation angles of α for $Sc_3C_2@C_{80}$ and $Sc_3N@C_{80}$.
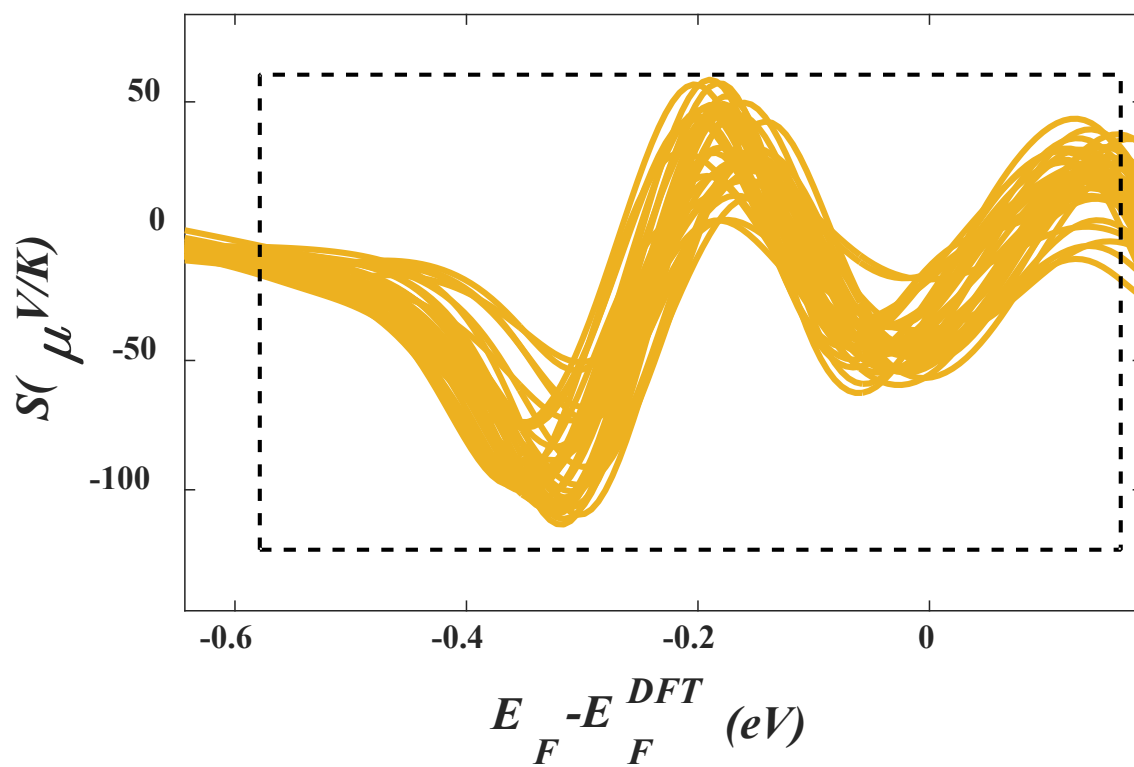
Figure S36. Seebeck coefficient S as a function of Fermi energy at 60 different orientation angles α of $Sc_3C_2@C_{80}$, for a tip-substrate distance of 2.5 Å.
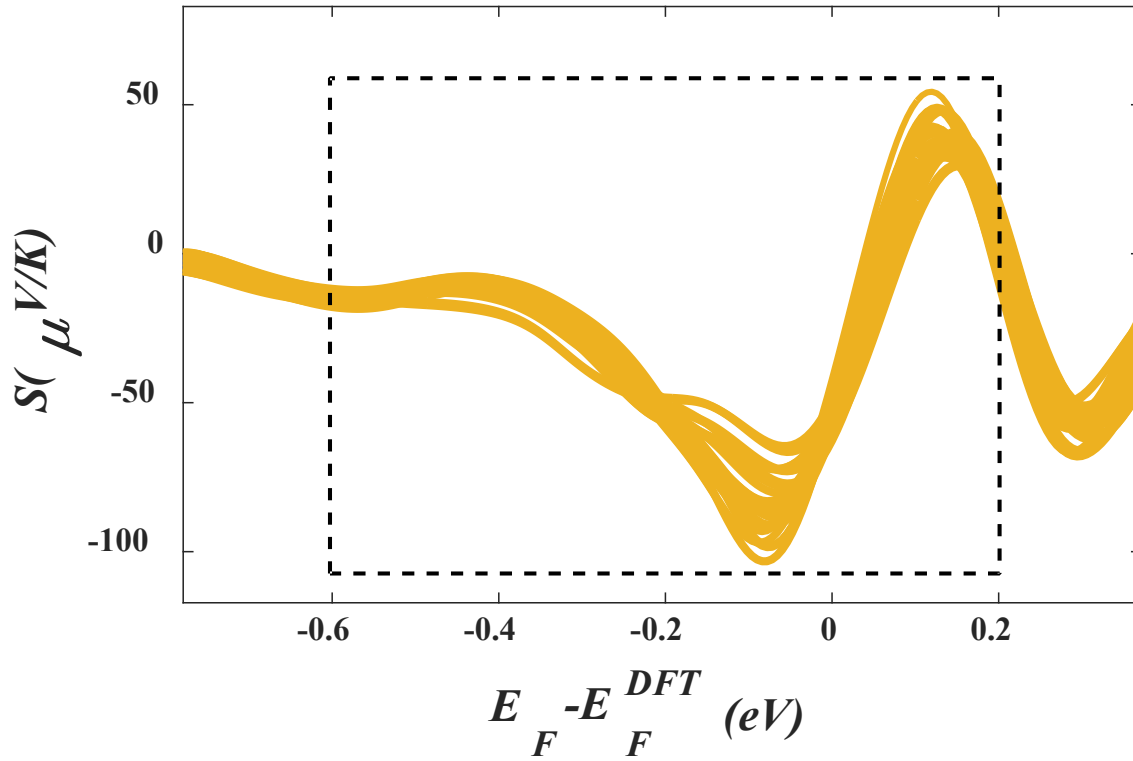
Figure S37. Seebeck coefficient S as a function of Fermi energy at 60 different orientation angles α of Sc$_3$N@C$_{80}$, for a tip-substrate distance of 2.5 Å.

5.13. Spin-dependent transport calculations in the vertical rotation axis (β)

In this section, we repeat the same calculations described in section 5.7, using the vertical rotation axis (β), as shown in Figure S38. As expected, the difference in the transmission coefficients is the smallest when the EMF rotates in vertical axis, and this is due to the fact that the distance between the metallic part Sc$_3$C$_2$/Sc$_3$N and the cage C$_{80}$ is kept the same. Figures S39 and S40 show small effect in the transmission curves while rotating in vertical axis (β), unlike in the horizontal axes θ and Φ. Since the rotation in this axis (β) has the smallest effect on the transmission coefficient curves one would expect the Seebeck coefficient S to be approximately similar for all rotation angles (see Figures S41 and S42 in the next section).
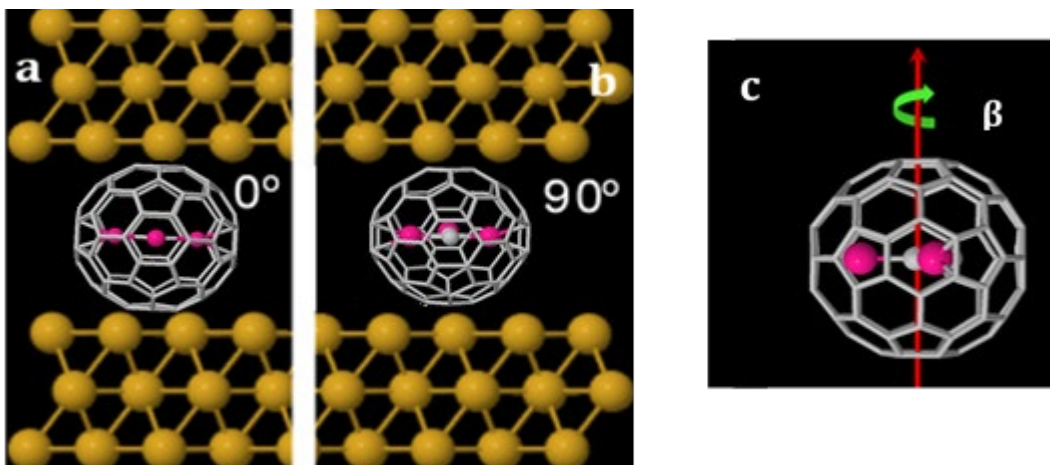
Figure S38. $Sc_3C_2@C_{80}$ between gold surfaces. **(a-b)**: The orientation of the $Sc_3C_2@C_{80}$ molecule with respect to the gold leads. **(c)**: The vertical rotation axis β.
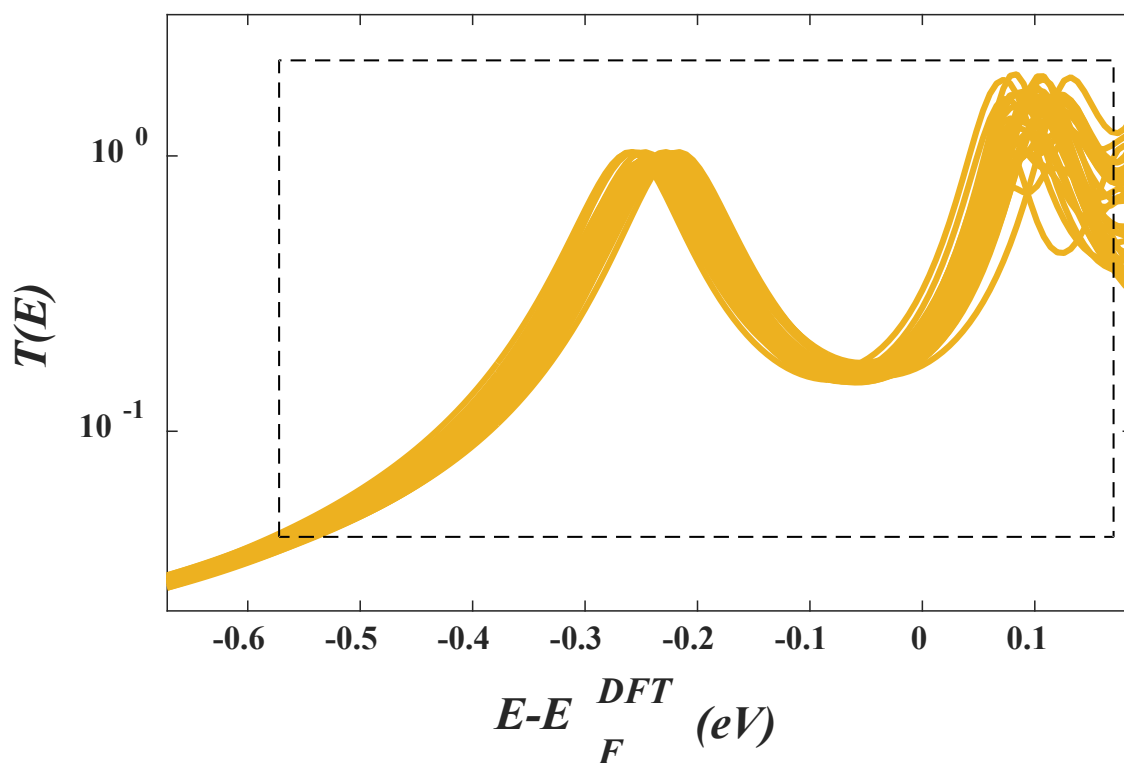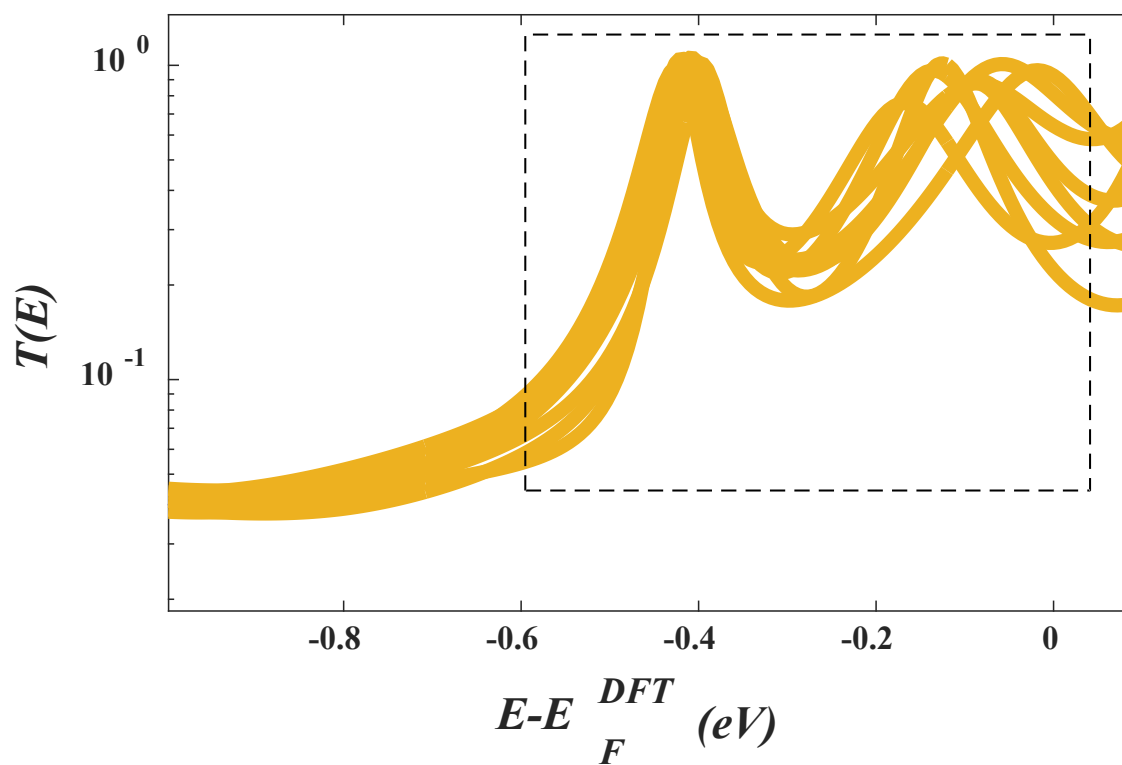

Figure S39. Spin-polarised transmission coefficients, $T(E) = \frac{T_{up}(E) + T_{down}(E)}{2}$, for the binding configurations of differnt orientations β of $Sc_3C_2@C_{80}$, and z = 2.5 Å.
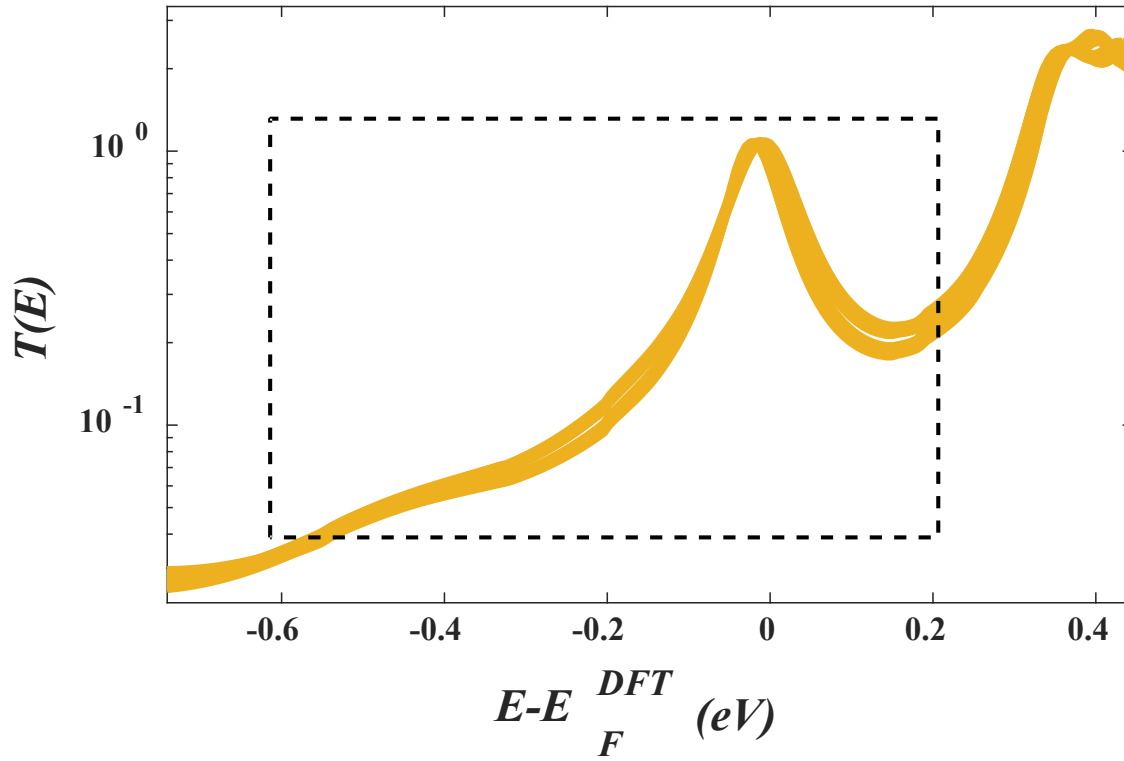
Figure S40. Spin-polarised transmission coefficients, $T(E) = \frac{T_{up}(E)+T_{down}(E)}{2}$, for the binding configurations of differnt orientations β of $Sc_3N@C_{80}$, and z = 2.5 Å.

5.14. Calculated Seebeck coefficient as a function of orientation in the vertical rotation axis (β)

Figures S41 and S42 show the average Seebeck coefficient S evaluated at room temperature for different orientation angles of β for $Sc_3C_2@C_{80}$ and $Sc_3N@C_{80}$.
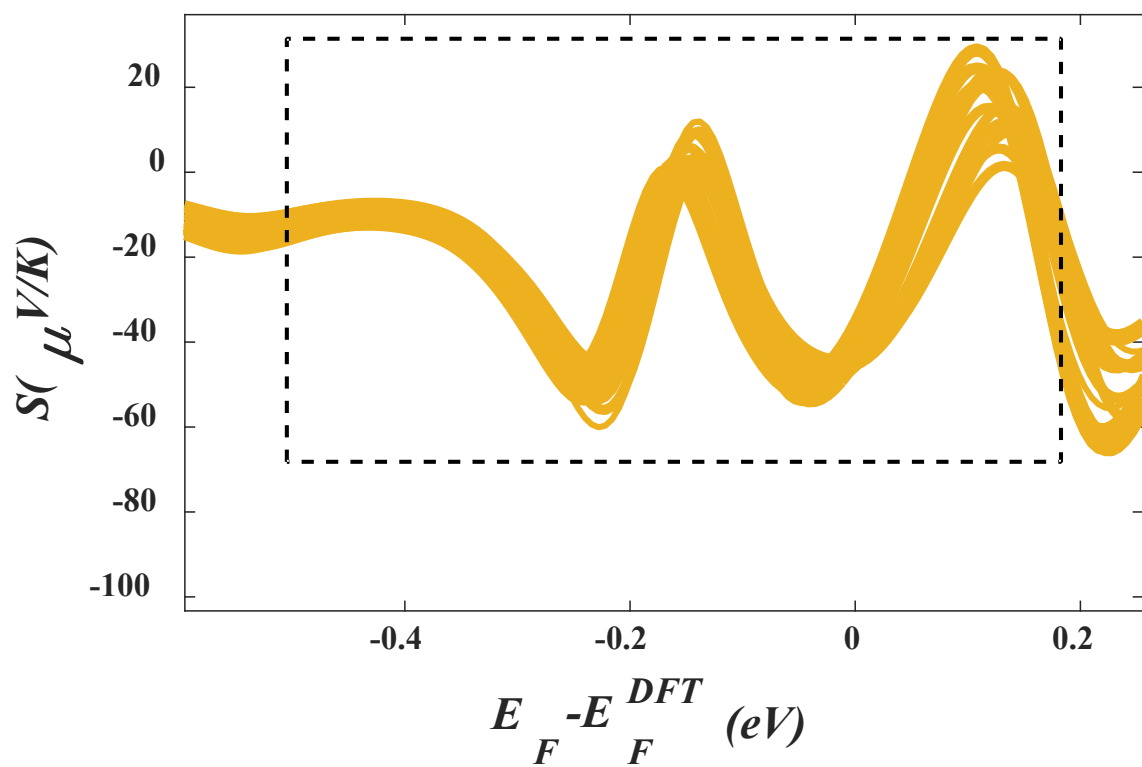
Figure S41. Seebeck coefficient S as a function of Fermi energy at 60 different orientation angles β of $Sc_3C_2@C_{80}$ for a tip-substrate distance of 2.5 Å.
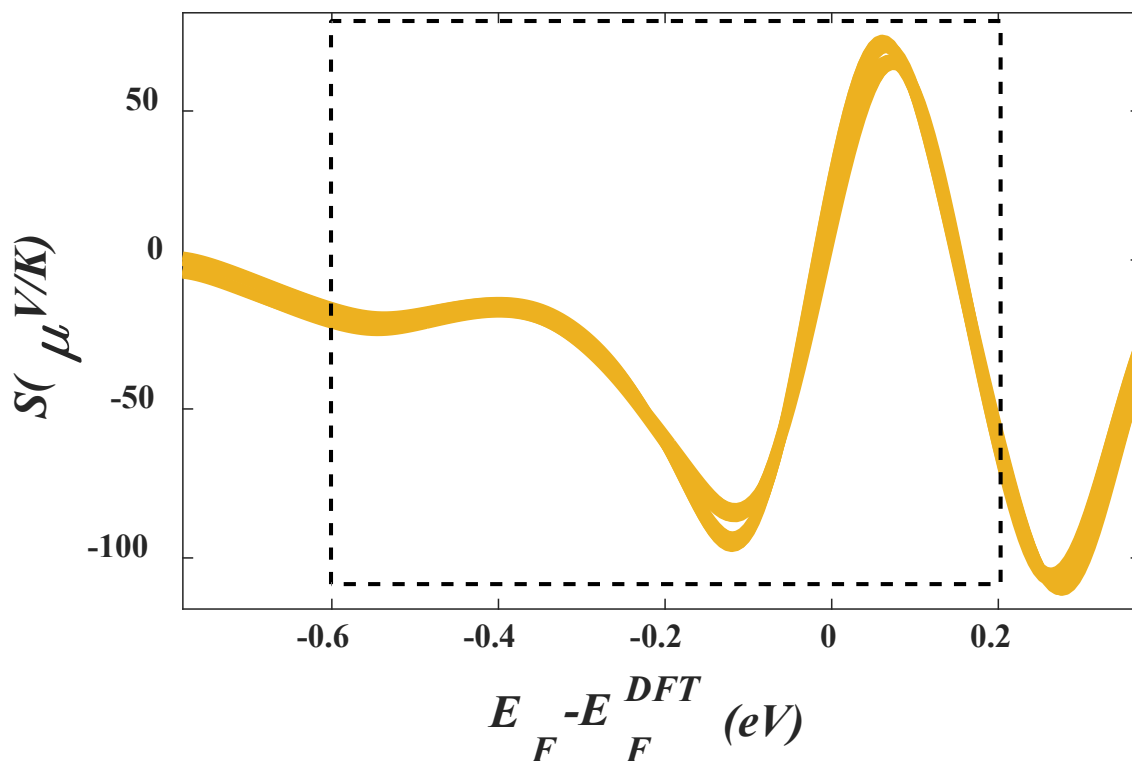
Figure S42. Seebeck coefficient S as a function of Fermi energy at 60 different orientation angles β of $Sc_3N@C_{80}$ for a tip-substrate distance of 2.5 Å.

5.15. Spin-independent transport calculations of C_{60}

In this section, we repeat the same calculations described in section 5.7, but for an empty cage C_{60}. Since C_{60} has no metallic atoms there is no need for spin-dependent calculations. As expected, the transmission coefficients are almost independent of the rotation angle about a vertical or horizontal axis, because the distance between the carbon atoms of the cage and Au-electrodes are almost unchanged by such rotations. Figure S43 shows no significant effect in the transmission curves while rotating about vertical or horizontal axis. Since the rotation has a negligible effect on the transmission coefficient curves one would expect the Seebeck coefficient S to be approximately similar for all rotation angles (see Figure S44). It is worth mentioning, due to the absence of the extra resonance caused by the metallic moiety (C_{60} is an empty cage), that the Seebeck coefficient S does not switch sign under rotation and is negative as shown in dashed-black square of Figure S44.

**Figure S43.** Spin-nonepolarised transmission coefficients, $T(E)$, for 60 binding configurations and, in different orientations around θ, Φ, β axes of C_{60}, and $z = 2.5$ Å.
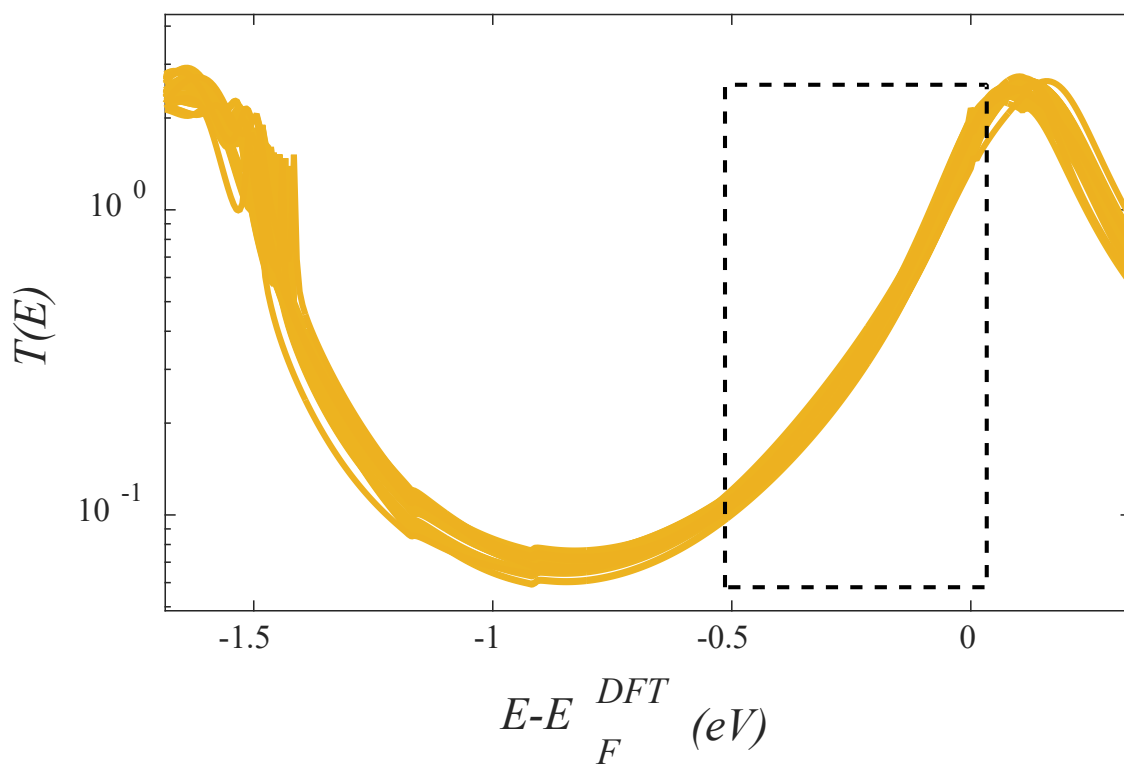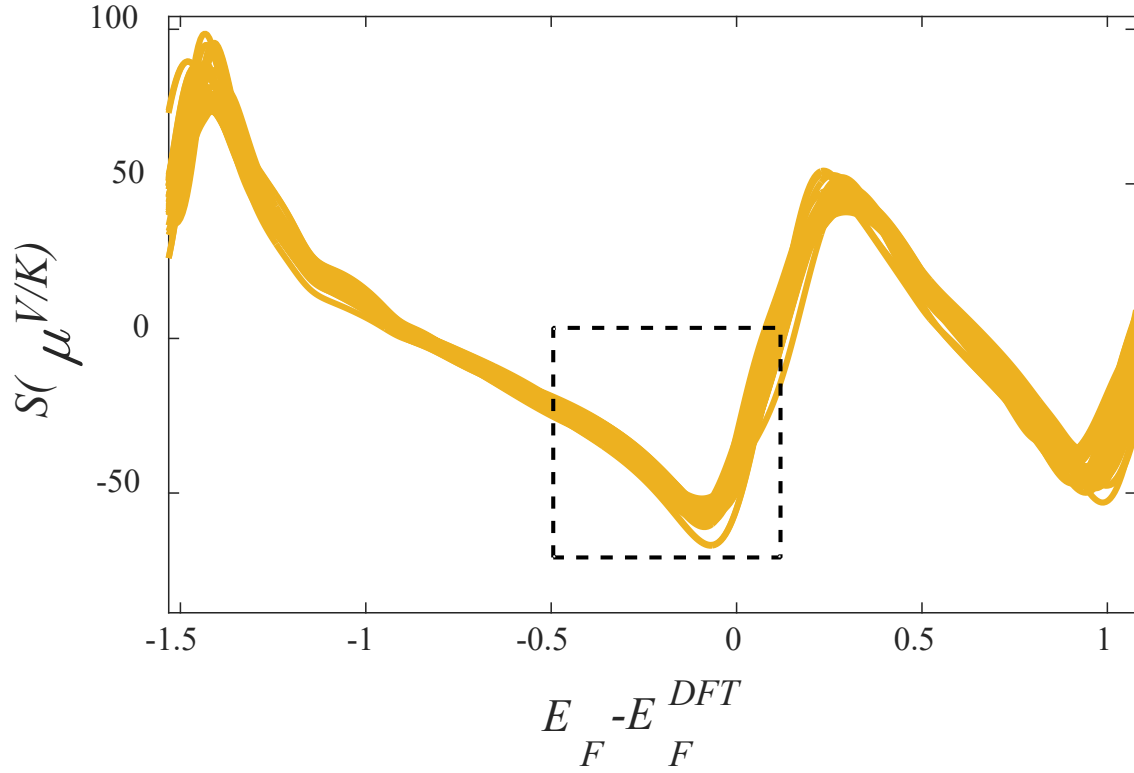
Figure S44. Seebeck coefficient S as a function of Fermi energy at 60 different orientations around θ, Φ, β axes of C_{60}. S versus Fermi energy at different orientation angles for a tip-substrate distance of 2.5 Å.

5.16. Standard deviation σ of $T(E)$ of EMFs and C_{60} in four different rotation axes

Table S4 contains the standard deviations σ (see Equation S6) of the transmission coefficient $T(E)$, in four different rotation axes θ, Φ, α and β, for two EMFs $Sc_3N@C_{80}$ and, $Sc_3C_2@C_{80}$ and the C_{60} fullerene. The standard deviation σ of the four axes follows $\sigma_\theta > \sigma_\Phi > \sigma_\alpha > \sigma_\beta$ for $Sc_3N@C_{80}$ and $Sc_3C_2@C_{80}$. This order is clearly shown in the transmission coefficient Figures S24-S43, whereas σ of the vertical and horizontal rotation axes are approximately equal ($\sigma_\theta \approx \sigma_\alpha$) for C_{60}.

$$\sigma = \sqrt{\frac{1}{n-1}\sum_{i=1}^{n}(x_i - \bar{x})^2} \tag{S6}$$

where $\bar{x}$ is the mean

$$\bar{x} = \frac{1}{n}\sum_{i=1}^{n} x_i$$

Similarly, Table S5, contains the standard deviations σ of the Seebeck coefficient S for four different rotation axes θ, Φ, α and β, for two EMFs $Sc_3N@C_{80}$, $Sc_3C_2@C_{80}$ and C_{60} fullerene. The standard deviation σ of the four axes follows $\sigma_\theta > \sigma_\Phi > \sigma_\alpha > \sigma_\beta$ for $Sc_3N@C_{80}$ and $Sc_3C_2@C_{80}$. This order is clearly shown in the Seebeck coefficient plots (Figures S26-S44), whereas for C_{60}, σ of the vertical and horizontal rotation axes are approximately equal ($\sigma_\theta \approx \sigma_\alpha$).

Table S4. Standard deviations σ of $T(E)$ in four different rotation axes θ, Φ, α and β, for two EMFs $Sc_3N@C_{80}$, $Sc_3C_2@C_{80}$ and C_{60} fullerene. Energy ranges (0.18 to -0.6), (0.18 to -0.38) and (0.0 to -0.5) eV of $Sc_3N@C_{80}$, $Sc_3C_2@C_{80}$ and C_{60}.

	$T(E)$				
Molecule	σ_θ	σ_Φ	σ_α	σ_β	Order
$Sc_3N@C_{80}$	1.374e-01	1.086e-01	1.045e-01	2.411e-02	$\sigma_\theta > \sigma_\Phi > \sigma_\alpha > \sigma_\beta$
$Sc_3C_2@C_{80}$	2.028e-01	1.887e-01	1.406e-01	3.158e-02	$\sigma_\theta > \sigma_\Phi > \sigma_\alpha > \sigma_\beta$
C_{60}	7.256e-02	==	4.873e-02	==	$\sigma_\theta \approx \sigma_\alpha$

Table S5. Standard deviations σ of _S_ in four different rotation axes θ, Φ, α and β, for two EMFs $Sc_3N@C_{80}$, $Sc_3C_2@C_{80}$ and C_{60} fullerene.

	S (μV/K)				
Molecule	σ_θ	σ_Φ	σ_α	σ_β	Order
$Sc_3N@C_{80}$	4.48e+01	1.83e+01	2.19e+01	4.55	$\sigma_\theta > \sigma_\Phi > \sigma_\alpha > \sigma_\beta$
$Sc_3C_2@C_{80}$	3.99e+01	2.83e+01	1.89e+01	1.23e+01	$\sigma_\theta > \sigma_\Phi > \sigma_\alpha > \sigma_\beta$
C_{60}	2.77	==	2.77	==	$\sigma_\theta \approx \sigma_\alpha$

5.17. Conductance G and thermopower S histograms of $Sc_3N@C_{80}$, $Sc_3C_2@C_{80}$ EMFs and C_{60}

In this section, we construct theoretical histograms of conductance G and Seebeck coefficient S by sampling the above results for $S(E_F)$ over Fermi energies within a range of 0.18 to -0.6 eV, centred on the metallic LUMO resonance DFT-predicted (see the black-dashed rectangle in Figure S24) for $Sc_3C_2@C_{80}$. Similarly for $Sc_3N@C_{80}$ the Fermi energies within a range of 0.18 to -0.38 eV, centred on the matallic LUMO resonance DFT-predicted (see the black-dashed rectangle in Figure S25). For C_{60} there is no metallic LUMO resonance, however, the Fermi energies within a range of 0.0 to -0.5 eV have been considered (the black-dashed rectangle in Figure S43).

In Figure S45 the theoretical histograms of conductance G against Seebeck coefficient S are shown. These calculations were taken in a range of Fermi energies of 0.18 to -0.6, 0.18 to -0.38 and 0.0 to -0.5 eV for $Sc_3C_2@C_{80}$, $Sc_3N@C_{80}$ and C_{60}, respectively. Figure S45 clearly shows that the Seebeck coefficient of $Sc_3C_2@C_{80}$ is larger than that of $Sc_3N@C_{80}$. These results are supported by experimental results as shown in Figure 2.
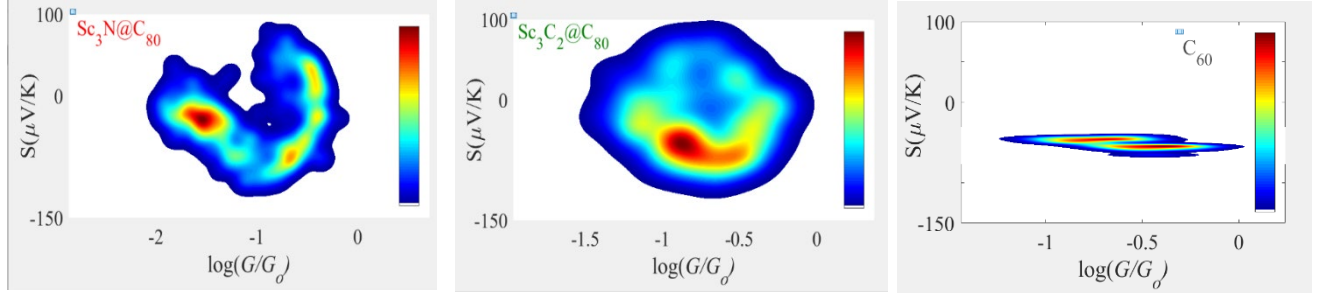

Figure S45. Theoretical histograms of conductance G against Seebeck coefficient S. Three ranges of Fermi energies (0.18 to -0.6), (0.18 to -0.38) and (0.0 to -0.5) eV considered for $Sc_3C_2@C_{80}$, $Sc_3N@C_{80}$ and C_{60}, respectively.

5.18 Power Factor

In this section, the power factor is calculated for $Sc_3C_2@C_{80}$, $Sc_3N@C_{80}$ and C_{60} within the same Fermi energy ranges for the four rotation axes and histograms generated. Since the conductance and Seebeck coefficient are calculated for a range of rotation angles for both $Sc_3C_2@C_{80}$ and $Sc_3N@C_{80}$, the power factor is calculated for the same angles. The black-curves in Figure S46 show distributions obtained from a fit uing the Kernel Density Estimation (KDE) in MATLAB.
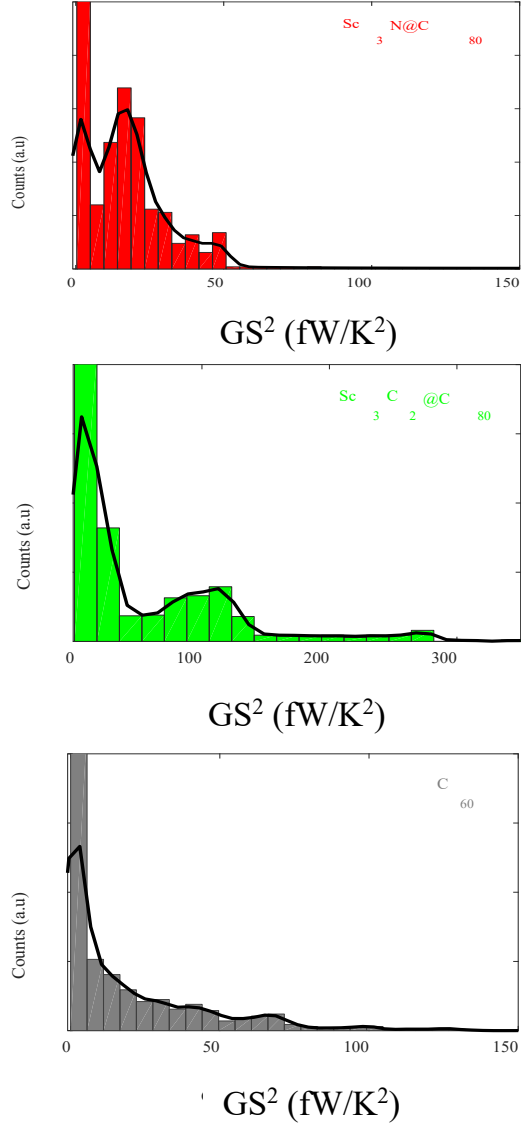
Figure S46. Theoretical power factor histograms for $Sc_3N@C_{80}$ (red histogram), $Sc_3C_2@C_{80}$ (green histogram), and C60 (grey histogram). The black lines show distributions obtained from a Kernel Density Estimation (KDE) in MATLAB.

5.19 Charge inhomogeneity

To characterize the charge inhomogeneity of each fullerene cage, we now compute the standard deviations of their charge distributions. If the charge on atom i is $|e|n_i$, then the standard deviation σ_q in the charge is defined by

$$\sigma_q^2 =< (n_i -< n_i >)^2 > \qquad (S8)$$

where angular brackets denote an average over all atoms on the cage.

51

Using DFT SIESTA code, we calculate the number of electrons n_i on each cage atom i in the gas phase for $Sc_3C_2@C_{80}$, $Sc_3N@C_{80}$, $Er_3N@C_{80}$ and C_{60} by three methods: Mulliken[11], Voronoi[12] and Hirshfeld charge[13]. Voronoi and Hirshfeld charges are more reliable than Mulliken charges, especially for large basis sets. Table S6 shows the number of electrons on the fullerene cage for $Sc_3C_2@C_{80}$, $Sc_3N@C_{80}$, $Er_3N@C_{80}$ and C_{60} in gas phase (as isolated molecule). The number of electrons on the cage atoms vary from one molecule to another, depending on the number of atoms in the metallic moiety and the nature of these atoms.

Table S6: Standard deviations of charge, conductance and Seebeck coefficient of $Sc_3C_2@C_{80}$, $Sc_3N@C_{80}$, $Er_3N@C_{80}$ and C_{60}. Charges are calculated using Mulliken, Hirshfeld and Voronoi methods. The values shown for the conductance are geometric standard deviations.

Molecule	Charge homogeneity (no. of electrons)			Conductance (G/G$_o$)		Seebeck (µV/K)	
	$\sigma_{Mulliken}$	$\sigma_{Hirshfeld}$	$\sigma_{Voronoi}$	σ_G Exp.	σ_G Theo.	σ_S Exp.	σ_S Theo.
$Sc_3C_2@C_{80}$	0.0154	0.0113	0.0133	2.00	4.56	19.2	36.0
$Sc_3N@C_{80}$	0.0163	0.0109	0.0119	2.34	5.58	17.6	29.4
$Er_3N@C_{80}$	0.00378	0.00259	0.00268	2.00	===	7.7	==
C_{60}	1.3e-04	5.7e-04	8.5e-04	1.86	2.23	6.8	2.44

References

1. Evangeli, C.; Gillemot, K.; Leary, E.; Gonzalez, M. T.; Rubio-Bollinger, G.; Lambert, C. J.; Agrait, N., Engineering the thermopower of C60 molecular junctions. *Nano letters* **2013,** *13* (5), 2141-2145.
2. Cusack, N.; Kendall, P., The Absolute Scale of Thermoelectric Power at High Temperatwe. **1958**.
3. Rincón-García, L.; Ismael, A. K.; Evangeli, C.; Grace, I.; Rubio-Bollinger, G.; Porfyrakis, K.; Agraït, N.; Lambert, C. J., Molecular design and control of fullerene-based bi-thermoelectric materials. *Nature materials* **2016,** *15* (3), 289-293.
4. Nečas, D.; Klapetek, P., Gwyddion: an open-source software for SPM data analysis. *Open Physics* **2012,** *10* (1), 181-188.
5. Soler, J. M.; Artacho, E.; Gale, J. D.; García, A.; Junquera, J.; Ordejón, P.; Sánchez-Portal, D., The SIESTA method for ab initio order-N materials simulation. *Journal of Physics: Condensed Matter* **2002,** *14* (11), 2745.
6. Herrer, I. L.; Ismael, A. K.; Milan, D. C.; Vezzoli, A.; Martín, S.; González-Orive, A.; Grace, I.; Lambert, C.; Serrano, J. L.; Nichols, R. J., Unconventional single-molecule conductance behavior for a new heterocyclic anchoring group: pyrazolyl. *The journal of physical chemistry letters* **2018,** *9* (18), 5364-5372.
7. Ismael, A. K.; Wang, K.; Vezzoli, A.; Al-Khaykanee, M. K.; Gallagher, H. E.; Grace, I. M.; Lambert, C. J.; Xu, B.; Nichols, R. J.; Higgins, S. J., Side-Group-Mediated Mechanical Conductance Switching in Molecular Junctions. *Angewandte Chemie International Edition* **2017,** *56* (48), 15378-15382.

8. Markin, A.; Ismael, A. K.; Davidson, R. J.; Milan, D. C.; Nichols, R. J.; Higgins, S. J.; Lambert, C. J.; Hsu, Y.-T.; Yufit, D. S.; Beeby, A., Conductance Behavior of Tetraphenyl-Aza-BODIPYs. *The Journal of Physical Chemistry C* **2020,** *124* (12), 6479-6485.

9. Lof, R.; Van Veenendaal, M.; Koopmans, B.; Jonkman, H.; Sawatzky, G., Band gap, excitons, and Coulomb interaction in solid C 60. *Physical review letters* **1992,** *68* (26), 3924.

10. Hung, Y.-C.; Jiang, J.-C.; Chao, C.-Y.; Su, W.-F.; Lin, S.-T., Theoretical Study on the Correlation between Band Gap, Bandwidth, and Oscillator Strength in Fluorene-Based Donor– Acceptor Conjugated Copolymers. *The Journal of Physical Chemistry B* **2009,** *113* (24), 8268-8277.

11. Mulliken, R., Electronic population analysis on LCAO–MO molecular wave functions. II. Overlap populations, bond orders, and covalent bond energies. *The Journal of Chemical Physics* **1955,** *23* (10), 1841-1846.

12. Bickelhaupt, F.; van Hommes, N., Organometallics1996, 15, 2923. Fonseca Guerra, C.; Handgraaf, JW; Baerends, EJ; Bickelhaupt. *J. Comput. Chem* **2004,** *25*, 189.

13. Hirshfeld, H., Synthesis, Crystal structure, and Hirshfeld Surface Analysis of a New Mixed Ligand Copper (II) Com-plex. *Theor. Chim. Acta* **1977,** *44*, 129-138.